



SAPIENZA
UNIVERSITÀ DI ROMA

Facoltà di Ingegneria Civile e Industriale

Dipartimento di Ingegneria Meccanica e Aerospaziale

Corso di Laurea Magistrale in Ingegneria Spaziale ed Astronautica

*Bistatic optical measurements for dynamic
characterization of LEO objects*

Tesi di Laurea

Relatore: Prof. Fabrizio Piergentili

Candidato: Lorenzo Mariani

Anno Accademico 2020/2021

1. Introduction

The increase of artifacts placed in orbit every year exponentially affects the amount of space debris surrounding the Earth. The European Space Agency (ESA) has estimated that currently, there are about 750,000 orbiting debris larger than 1 cm [1], this situation worries both the space agencies of any country and the private industry operating in the aerospace sectors because possible collisions in flight between their systems and a debris swarm [2, 3].

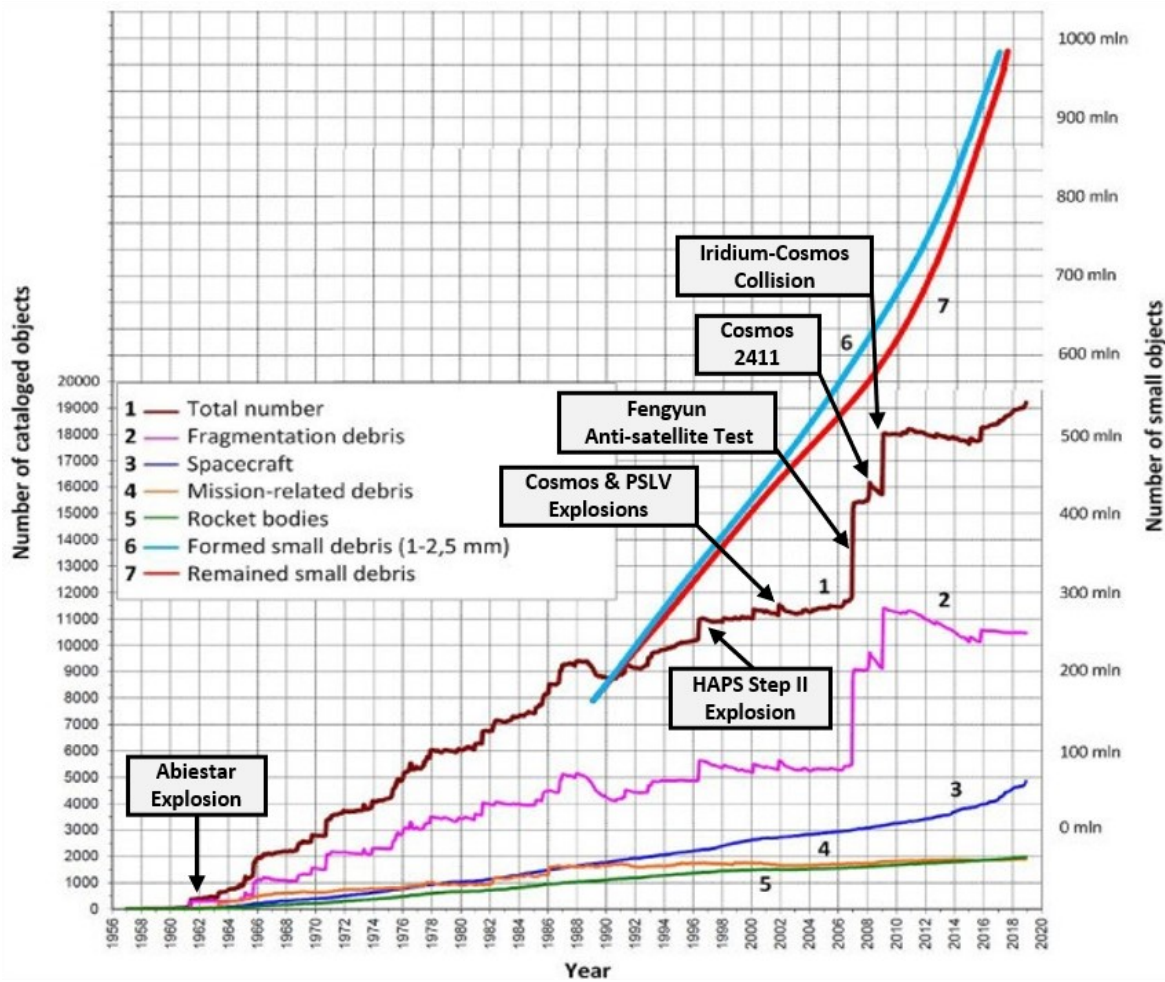


Fig. 1 – Number of catalogued object over time [4].

Current technology does not allow the removal of uncontrolled debris from orbit but only its monitoring and over the years, a large amount monitoring system have been developed which allowed to track and catalogue about 23'000 uncontrolled object [1].

Dimension	Number of objects	Trackable
1 mm – 3 mm	Millions	No
3 mm – 1 cm	Millions	No
1 cm – 5 cm	500k (estimated)	No
5 cm – 10 cm	Thousands	No
> 10 cm	Hundreds	Yes

Tab. 1 - Space debris numbers by dimension [1]

Nowadays, the most comprehensive and available catalogue of uncontrolled objects is the North American Aerospace Defence Command (NORAD) one. The American institution releases periodically orbital information about the objects in the form of Two Line Elements (TLE), which report, ordered in two strings of code, both a set of Kozai-Brouwer mean orbital elements and a term BSTAR (B^*) referred to the area over mass ratio [5]. Unfortunately, the TLEs cannot be used in Space Surveillance and Tracking (SST) as they characterize the orbital motion of tracked object in a purely theoretical model, which accumulate, during each single orbit, the sum of all the variables not considered by the ideal model [6]. For this reason, after a certain period, the errors accumulated by the TLE become so large that they no longer describe the orbit of the tracked object involving an inaccuracy such to update them through a new series of direct measurements and a consequent release of new TLEs after few hours [7, 8]. Due to the huge number of probabilistic variables that contribute to changing the orbit of an object, any predictive model developed will never describe the rigorous behaviour of the object. Today the research is oriented towards continuous and frequent direct measurements of debris which allow both to know the position of the object with very low margins of error and to contribute to the development of innovative techniques aimed at improving existing mathematical models. The knowledge of the state of the object is fundamental to understand the behaviour of the object itself, therefore it must be observed. Many observation systems are used for the observation of debris and their direct measurement: laser, radar and optical systems. Nowadays, the most

advanced technique used for tracking space debris is their simultaneous optical observation through a network of observatories. Multi-site optical observation has been developed to increase quality of optical measurements by using at least two optical instruments which acquire data from the same object at the same time. Optical measurements obtained from the different observers allow to reconstruct the objects' attitude and the determination of their positions in the 3D space, providing a direct estimation of their altitudes. Altitude and attitude of the object are crucial parameters during the re-entry into the atmosphere. In the re-entry phase, both parameters are subjects to variations due unpredictable factors. The acquisition of more data in a short interval of time is necessary to predict their evolution with better precision. The factors that more heavily contributes to the deviation between the predicted and the real trajectory are the ballistic coefficient and atmospheric density. The first is determined from the attitude, while the latter depends on solar activity, different concentration of chemical species and other factors which lead to inaccuracies in the various theoretical models. In general, in an object's re-entry phase there are few chances to observe it from the same observatory. This is due to low revisit time, which does not allow frequent opportunities of visibility and meteorological factors. During these few visible passages, is then necessary to acquire large data sets with high accuracy which are then to be used to provide the most accurate prevision in attitude and position.

In this thesis will be discuss a set of innovative techniques which, by exploiting direct optical observations, allow to derive the flight attitude of uncontrolled object. In particular, will be discussed a methodology which allows to obtains the "light-curves" from direct optical observations of an object (satellite or debris), acquired from different observatories at same time (simultaneous multi-site observation) and how, through their inversion, it will be possible to derive the attitude dynamics of its. The knowledge of the attitude dynamics makes it possible to significantly improve the terms related to the atmospheric drag responsible for the orbital degradation of any orbiting object and, consequently, the predictive models can also be improved. Furthermore, performing simultaneous multi-site observation drastically reduce the error about flight level altitude and allows to attribute

very precisely the term related to the effect of atmospheric drag at the observed debris. In these years Sapienza Space System and Space Surveillance (S5Lab) got experience in satellite systems manufacturing and launch and in the space debris field [9-19], operating network [20-26] of completely remote optical observatories, capable to observe, catalogue and identify a huge number of objects both known that unknown, thanks to which it was possible to refine the correlation between light curves and attitude dynamics of the observed debris. For these reasons every methodology discussed in this thesis is strongly based on a great number of observations which permits to obtain reliable and solid results.

2. Light-curve approach for SSA and SST support

The alarming recent increase in the population of satellites and space debris in Earth orbit has caused overcrowding in highly desirable operating regions. The government's cataloguing, analysis and alarm systems are becoming overwhelmed and inadequate to manage the current condition. It appears that operations taking place in orbit, which are currently safe, may be at risk.

Space Traffic Management (STM) has two main objectives: to improve the knowledge of behaviour, the cataloguing and monitoring of space debris, and to improve the prevention of collisions in orbit. In this way it is also possible to obtain greater safety for manoeuvres at close range and to increase the reliability of alarms for collision events. As the different orbital bands become increasingly more crowded, and the number of objects passing from one band to another consequently increases, the ability to successfully predict potential collisions and to take action to avoid them is essential. Predicting these events requires adequate data, advanced algorithms, identification and tracking techniques.

An effective remediation measure in order to stabilize the population in Low Earth Orbit (LEO) include the active removal of large, massive space debris and collision avoidance by deviating the objects using, e.g., ground-based lasers. Both techniques require not only

precise knowledge of the target objects' orbits, but also of their attitude because, to accurately propagate the orbits of potential collision partners, non-conservative orbital perturbations — such as the pressure of solar radiation and atmospheric resistance, which depend on the attitude — must be known. The state of the object, which traditionally consists of position and speed, is certainly of interest, but additional information is also crucial. The so-called characterization information includes details about the attitude motion, shape and material of the space object.

One way to obtain the characterization information is through the light curves, which represent the change in brightness over time of the object. The reflected brightness received by an observer depends both on the geometry of the observation, therefore on the relative position between observer, object and Sun, but also on the properties of the object such as its attitude, its materials and its shape. Furthermore, light curves, are a technique useful to determine rotation or tumbling rates, as well as their temporal changes.

The first application in which light curves were widely used was to recover information on the shape of asteroids using different techniques [27-30]. In this case, simplifying assumptions can be used as asteroids usually have a rotation of the main axis and smooth surfaces made up of a single surface material, which greatly simplifies the inversion of their light curves. As for man-made space objects, such as satellites and space debris, many have a controlled attitude, which simplifies the problem of reversing their light curve. In general [31-33], it has been shown that no principal axis attitude movement can be assumed for uncontrolled spatial objects.

The light curve approach can be used for three different application:

- The first aims to obtain information on materials. Lynch et al. [34], Seitzer et al. [35] and Schildknecht et al. [36-38] analyzed respectively: GEO satellite surface material properties, classified GEO debris based on their size and color, and performed color photometry to distinguish GEO debris based on material types.

- The second is focusing on the study of the space objects tracklets and correlating with a priori knowledge. Cowardin et al. [39] compared optical measurement of Titan fragments with laboratory results to obtain the best match result. Scott et al. [40] established a light curve catalogue based on satellite bus types, and made the comparison to differentiate objects.
- The third is based on the directly shape inversion. Hall et al. [41] presented various methods of directly inverting the light curves of spatial objects in order to identify their approximate shape and attitude. To increase the accuracy of the results it was necessary to combine the data obtained with the light curves with the propagation of the orbit, since the problems are coupled [42]. This implies the resolution of a problem with a large number of parameters, which is often not easy to determine. Furfaro et al. [43], to solve this problem, he used machine learning in which Bayesian networks are formed. It is also possible to merge data from different sensors, using an unscented Kalman filter, in order to further increase the accuracy of the estimation of the characterization information. The latter method was proposed by Linares et al. [44, 45] who simulated several scenarios with success. Furthermore Piergentili, Santoni et al. have faced the problem of inversion of the light curves obtained from BVRI photometric observations of GEO [46] objects, and from optical observation of LEO satellite and space debris [47, 48]. For the latter, the observed light-curve is compared with a synthetic one in order to retrieve the object's attitude. Many synthetic light-curves are generated with different initial attitude parameters. The more the synthetic light-curve is similar to the observed one, the greater the likelihood that the corresponding attitude parameter represents the real object's attitude. Later, a genetic algorithm is used to minimize a cost function defined as the difference between the real light-curve and the synthetic one [49].

In conclusion, the study of light curves is a very versatile approach that can be used for different purposes. From the various studies carried out it is clear that the use of a network

of telescopes that aims to create a database of light curves can certainly be of support to the activities of Space Traffic Management (STM) and Space Situational Awareness (SSA).

3. System description

The S5Lab observatories network includes many telescopes in different country in the world [20]. To get the real light-curve presented in this thesis, the Remote Space Debris Observation System (RES DOS) and the Sapienza Coupled University Debris Observatory (SCUDO) observatories, located in Rome (RM) and Collepardo (FR) respectively, are used (Fig. 2). In both systems an sCMOS sensor is installed integrally with the main telescope and its mount, so the systems are able to track the satellite e contemporary acquire the video.



Fig. 2 - RES DOS and SCUDO observatories managed by S5Lab

The sCMOS sensor allows to obtain a readout rate greater than CCD sensor ensuring a large value of frame rate (fps). Moreover, the mount used to move the telescope are able to track every satellite in every orbital regime (LEO, MEO, GEO). Both systems are equipped with

the same sCMOS sensor and mount and in the following table a summary of the main characteristics of the two systems are indicated (Tab. 2):

RES DOS / SCUDO		
Sensor	Type	sCMOS
	Resolution	5.5 Mpx
	Sensor diagonal	22 mm
	Max fps	100
Telescope	Focal length	750 mm
	Diameter	150 mm
	Mount type	Equatorial

Tab. 2 - Main optical characteristics of RES DOS and SCUDO observatories

4. Object light-curve

The light-curve of the object is the variation over time of its apparent magnitude. To calculate the apparent magnitude of the object it is necessary to determine which stars are present in the field of view in each frame and therefore it is necessary to solve the stellar field of the images. The resolution of the stellar field is carried out thanks to the use of the Astrometry.net software [50] which outputs the resolved image, or the image in which are present the celestial coordinates for each pixel coordinate, and a text file. The text file contains information on the stars used to resolve the star field, they are present for each star: celestial coordinates, pixel coordinates and bolometric (B) and visual (V) catalogue magnitudes. The star catalogue used to solve the star field by Astrometry.net is the Tycho-2 [51]. The Tycho-2 Catalogue contains positions, proper motions and two-colour photometric data for the 2.5 million brightest stars in the sky. The magnitude errors is lower than 0.1 for stars with magnitude 10 and then gradually rises to at most 0.4 at magnitude 12 and fainter. The position and magnitude measurements of Tycho-2 stars are based on

observations made by the astronomical satellite Hipparcos, built by the European Space Agency in order to map the entire sky. The United States Naval Observatory (USNO) used Hipparcos data for the compilation of the Astrographic Catalog / Tycho Reference Catalog, including about one million stars, therefore the use of Tycho-2 was preferred both for the high number of stars than to be precise in terms of magnitude.

4.1. Reference star selection criterion

Many stars may be present in the field of view, but not all of them can be used as a reference for calculating the magnitude of the object. Moreover, to calculate the apparent magnitude of one star with respect to another, the two stars must be approximately of the same spectral class, that is, be of the same colour [52]. In Fig. 3 is shown how the mean and the standard deviation of the magnitude error decrease using stars with the same spectral class.

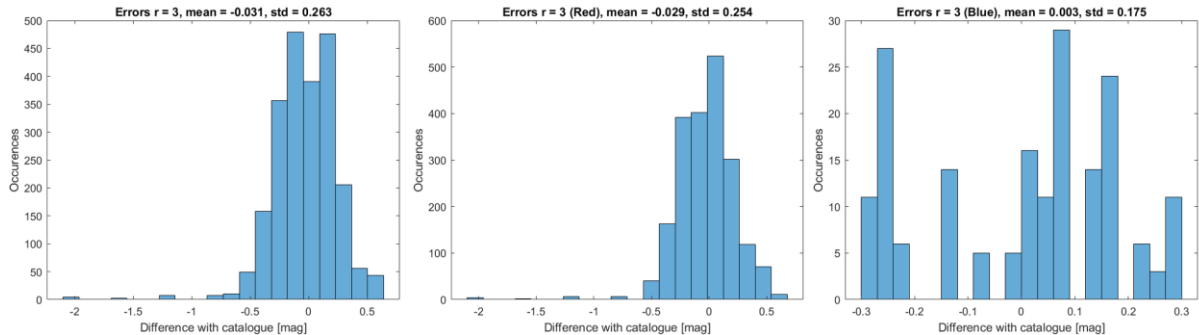


Fig. 3 - On the left is shown the histogram obtained using all the stars present in the video recording, on the centre using only the red stars and, on the right, using only the blue stars. The analysed video is composed by 1000 frames and is referred to the tracking of ATLAS 2AS CENTAUR (SSN 28096) taken the 30/10/2020 from RESDOS observatory.

The colour of the star can be determined from its temperature, and the temperature can be obtained through the knowledge of the difference between bolometric and visual magnitude (B-V).

$$T = \frac{7090}{(B - V) + 0.71} \quad (1)$$

It has been assumed that if $B-V < 0.3$ then the star is blue, otherwise red, since for $B-V = 0.3$ a star temperature of about 7000 K is obtained, which corresponds approximately to a white star (Fig. 4).

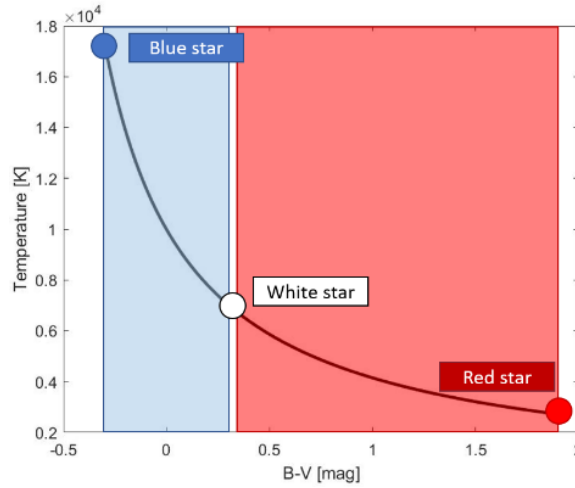


Fig. 4 - The figure shows the relation between the temperature and the difference between bolometric and visual magnitude

4.2. Image calibration

Before proceeding with the calculation of the intensity of the star, it is necessary to calibrate the image in order to correct phenomena due to the sensor such as the variation in quantum efficiency, vignetting, dark current, bias level and the gain for AD conversion. The applied method is known as standard calibration [53] which can be expressed as:

$$IMG_{corr} = \frac{\overline{MFF}}{MFF} (IMG_{raw} - MDF) \quad (2)$$

where IMG_{raw} indicates the original raw image, IMG_{corr} is the corrected image, MDF the Master Dark Frame, MFF the Master Flat Field frame and \overline{MFF} the average of the central

pixels of the *MFF*. From this expression it can be seen that if the image were uniform the term $\frac{\overline{MFF}}{MFF}$ would be equal to 1. The frames necessary for the standard calibration are obtained by following the following procedure:

1. Calculate the average or the median of a few dark frames obtained with a time integration equal to that used for the astronomical subject, thus obtaining the Master Dark Frame (MDF).
2. Calculate the mean or the median of a certain number of flat-field frames, thus obtaining the Master Flat-Field Frame which, however, has yet to be corrected by its Dark.
3. Dark frames are taken relative to flat-field frames, i.e. with a time integration equal to that used for the astronomical subject. The result is the Master Dark Frame of the Flat (MDFF).
4. The MDFF obtained at point 3 is subtracted from the master flat-field obtained at point 2, thus obtaining the Master Flat-field Frame (MFF).
5. The master dark frame is subtracted from the raw image of the astronomical subject obtained in step 1.
6. The average value of the pixels of the central area of the flat-field master obtained in point 4 is calculated (\overline{MFF}).
7. The image obtained at point 5 is divided, pixel by pixel, by the average obtained at point 6 and the MFF. The calibrated image was therefore obtained.

4.2.1. Dark frames

The dark frame is obtained by taking a photo in the dark and with the shutter closed. It is necessary to use the conditions that were, or will be, at the time of the integration of the astronomical subject. In particular, it is necessary that the temperature of the sensor during the resumption of the astronomical subject and that used to make the Darks is the same. For this reason, you run the dark just before or after the actual integration. The dark frame must

be obtained with an integration time exactly the same as that used to obtain the astronomical image. The dark frame it contains the thermal electrons accumulated during integration, but also the noise itself thermal and random variations in the number of accumulated thermal electrons, plus all elements contained in the bias frame. The Master Dark Frame used in this thesis was obtained by making the median of 200 dark frames (Fig. 5).

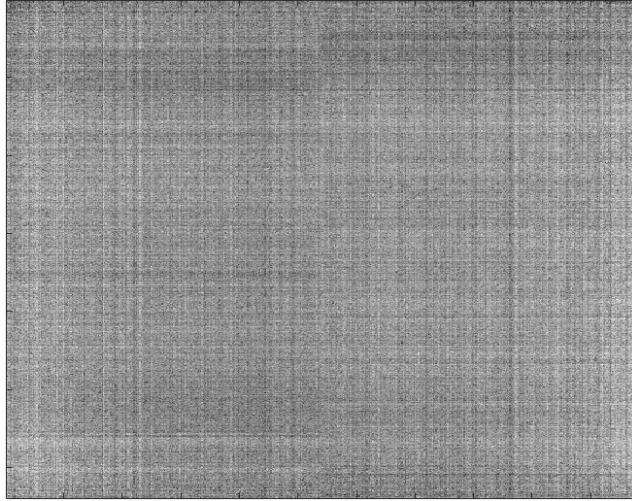


Fig. 5 - Master Dark Frame example taken by SCUDO observatory.

4.2.2. Flat-Field frames

The Flat-Field Frame is used to consider the variation in sensitivity (non-uniformity) of the pixels, the effects of any vignetting, specks of dust and dirt. These factors are not eliminated through the dark frame calibration, for this reason the optical system used for shooting the flat-field frame must be the same used for taking the astronomical image. So, by evenly illuminating the entire CCD sensor, what we get is a map of the sensitivity of the CCD, i.e. a map of the conversion efficiency of photons into electrons by each pixel. The flat-field frame can be obtained by taking a photo of a light source, so that the sensor is uniformly illuminated. This photo can be taken by taking a photo during sunset by placing a well-spread white sheet in front of the lens or by using a special tool for generating flat-field frames. The exposure time to be used is that necessary to obtain about 50% of the value necessary for sensor saturation. The Master Flat-Field used in this thesis was obtained by

making the median of 200 flat-field frames, from which the own Dark was subtracted, always obtained by making the median of 200 Darks relative to the flat-field frame (Fig. 6).

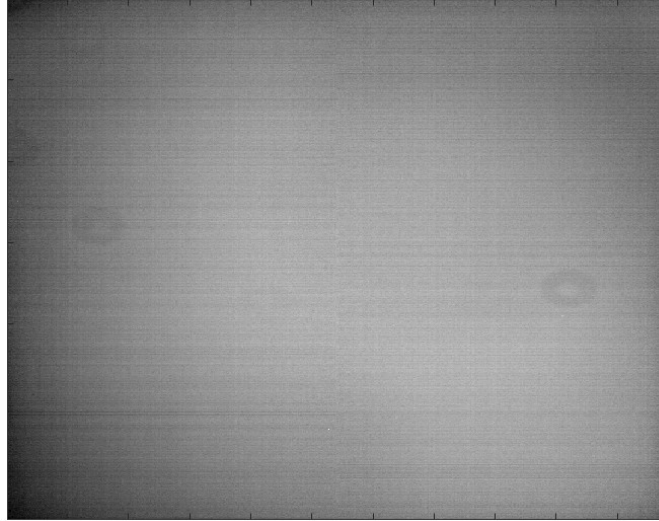


Fig. 6 - Example of Master Flat Field Frame taken by SCUDO observatory.

4.3. Aperture photometry

To calculate the apparent magnitude of a star it is necessary to know its intensity, in terms of Analog Digital Unit (ADU), the intensity of other stars and their catalogue magnitude. It is therefore necessary to calculate only the intensity of each star in the field of view since the magnitudes of the catalogue are already known. The procedure for calculating the intensity of the star (or of an object) is called aperture photometry [54] and mainly consists of four steps: image centring, estimation of the background (sky) level, calculation of the intensity and the estimation of the star radius. Since the pixel coordinates of the stars are already known, an algorithm for star centring is not necessary.

4.3.1. Background estimation

The estimation of the background level allows to correct the fact that the same pixels that collect photons of the object also collect photons from the sky. A common technique is to place a software annulus around the object with a total number of pixels about three times

the number contained within that of the source aperture [54]. For the pixels of the sky annulus the median intensity is found and then are tossed out all those with values greater than $\pm 3\sigma$ from the median. With this cut-off are eliminated the cosmic ray hits, bad pixels, and astronomical neighbours' contamination. The cut-off technique is repeated another time with the new distribution. Finally, the background level is the median value of the final histogram.

4.3.2. Star Intensity

For calculation of the star intensity a software aperture of star dependent radius is centred on the pixel coordinate of the star and then the pixels in this area (A) are summed; this is the total integrated photometric source signal (S). In order to remove the background, the following formula is applied:

$$I = S - n_{pix} * \bar{B} \quad (3)$$

Where n_{pix} is the total number of pixels contained within the area A and \bar{B} is the background level discussed above. With this value is possible to exclude all the stars that are saturated.

4.3.3. Star radius estimation

It has been shown by Howell [55] that exists a relation between the radius of the aperture of the star and the signal-to-noise ratio obtained for that measurement. An optimum of the radius aperture, that is, one that provides the optimum or best signal-to-noise ratio for the measurement, can be determined, and generally has a radius of near $1 \cdot \text{FWHM}$. This optimum radius is a weak function of the source brightness, becoming smaller in size for fainter sources. When the optimum star radius is found, it is possible to calculate the intensity of the star using this radius (Fig. 5-6).

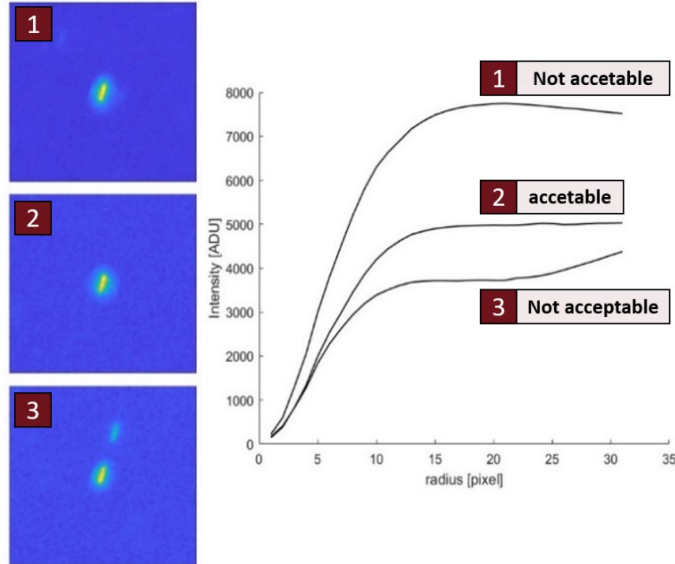


Fig. 7 - Grow curves for 3 different stars. The upper curve corresponds to the upper image, the central curve (the only one good) corresponds to the central image and the lower curve corresponds to the lower image.

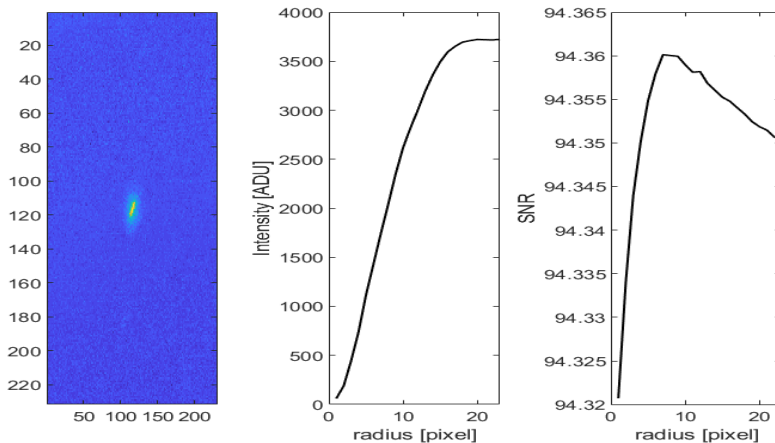


Fig. 8 - Star image on the left, grow curve in the center and the SNR curve calculated with the CCD equation in the right. From the last curve an optimum radius equal to 7 px is found.

In the example represented in Fig. 7 is shown how the mean and the standard deviation of the error in magnitude change according to a different value of the radius used for each star in each frame. The analysed video is the same indicated in Fig. 3 and a minimum in the standard deviation occurs for $r = 3$. This radius is the optimum value for the video analysis (Fig. 9).

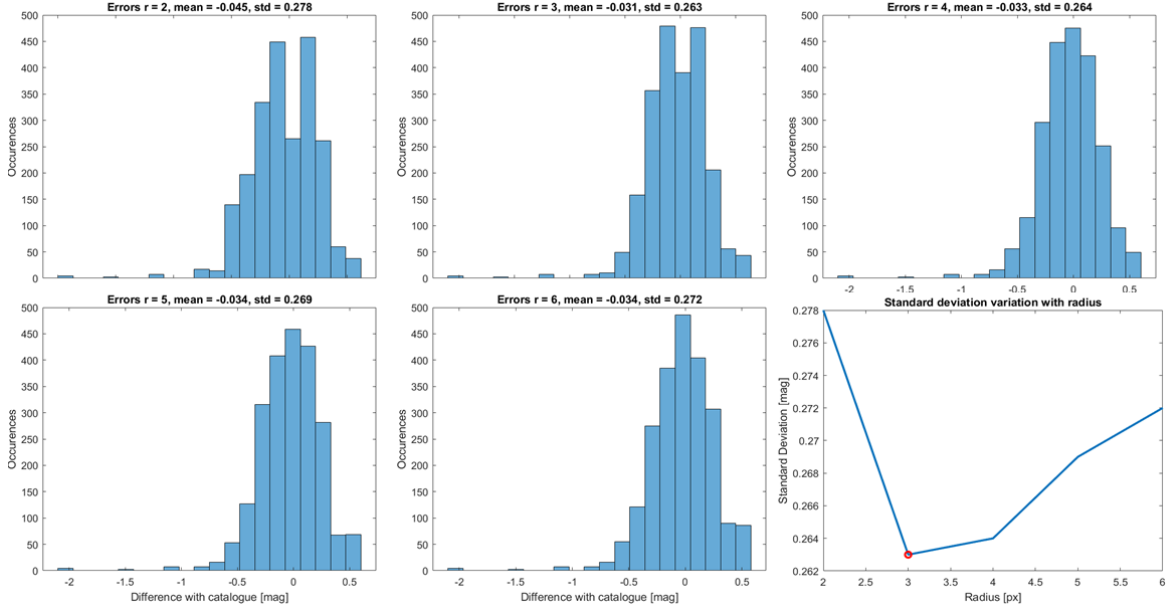


Fig. 9 - Optimum radius identification: standard deviation and mean of the error for each radius used for analysing the example video.

4.4. Stars magnitude

The previous procedure calculates the intensity of each star present in the field of view for each frame. Therefore, the intensity of each star is obtained as a function of time. Since the object is being chased, the latter will be stationary in the field of view, while the stars will move. Therefore, the same stars will not always be present during the entire recording of the object. The object video is then divided into time intervals. In each interval, only the stars that are present in the entire length of the interval are chosen. The intensity of the star is approximated as a constant that is equal to the median of the intensities that the star assumes in that interval. At this point, the apparent magnitude of each star present in the interval is calculated with respect to all the others present in the same interval by:

$$mag_{star_i} = mag_{star_{j,cat}} - 2.5 \log \left(\frac{I_{star_i}}{I_{star_j}} \right) \quad (4)$$

for $i, j = 1, \dots, star_{number}$ and $i \neq j$, where mag_{star_i} is the magnitude of the i-th star, mag_{star} is the catalogue magnitude of the j-th star, I_{star_i} is the intensity of the i-th star in ADU and I_{star_j} is the intensity of the j-th star in ADU. For each star, therefore, a vector of possible apparent magnitudes is obtained, and it is assumed that the apparent magnitude of the star is equal to the median of these values. In each interval there is a certain number of stars n , which are combined in groups of m , with $m \leq n$, in order to find the combination of m stars that minimizes the difference between the calculated magnitude and the catalogue magnitude. The set of combinations of stars chosen for each interval represents the list of stars that will be used as references for calculating the magnitude of the object being tracked.

4.5. Algorithm for video analysis

To calculate the change in magnitude of the tracked object over time (light-curve) it is necessary to calculate the intensity of the object in each frame. If the object is not perfectly still in the field of view during the recording, as often happens, it is necessary to use an algorithm that determines the pixel coordinates of the object centre in each frame. Once the coordinates of the object in each frame have been obtained, it is possible to calculate the intensity of the object as described in section 4.3.2 and consequently its magnitude as described in the previous section, using as reference stars those that result from the optimization process .

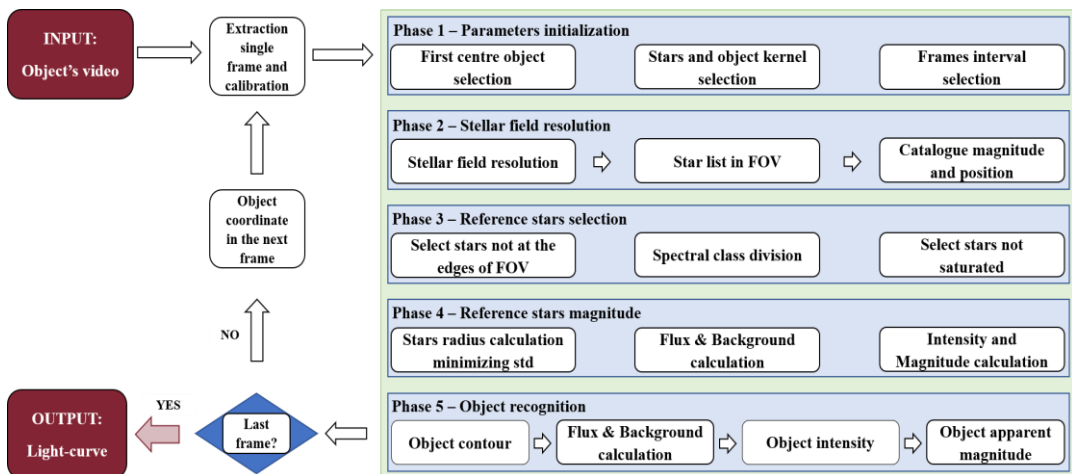
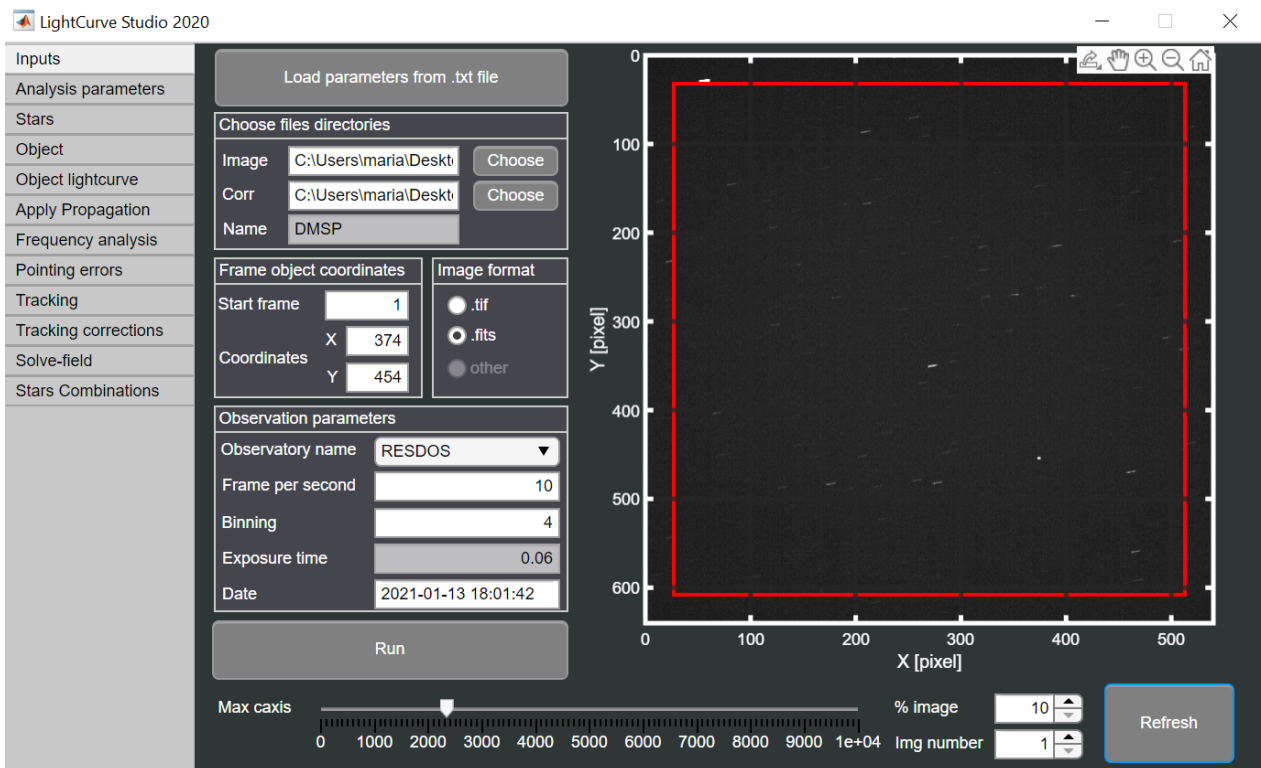


Fig. 10 - Video analysis software flow chart

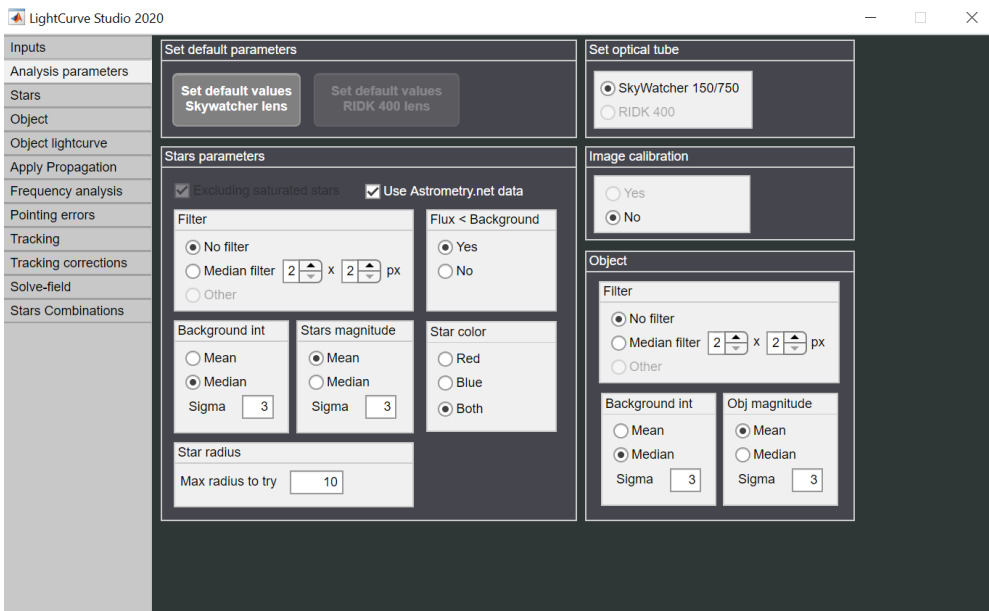
A MATLAB code with a graphical interface (GUI) was implemented in order to extract the light-curve and the flow-chart of the software is shown in Fig.10, while the Fig. 13 shows the various sub-sections (Tab) of the code in which the steps described in the previous flow chart are carried out.

4.5.1. Input tab



The images to be analyzed, and the respective text files containing the catalog magnitudes and the position of the stars, are entered as input. Here the user can also add further inputs, such as the time and date of the video, the observatory, the pixel coordinates of the object in the first frame to be analyzed and any binning. To get a better visualization, the image histogram can also be adjusted as needed.

4.5.2. Analysis parameters tab



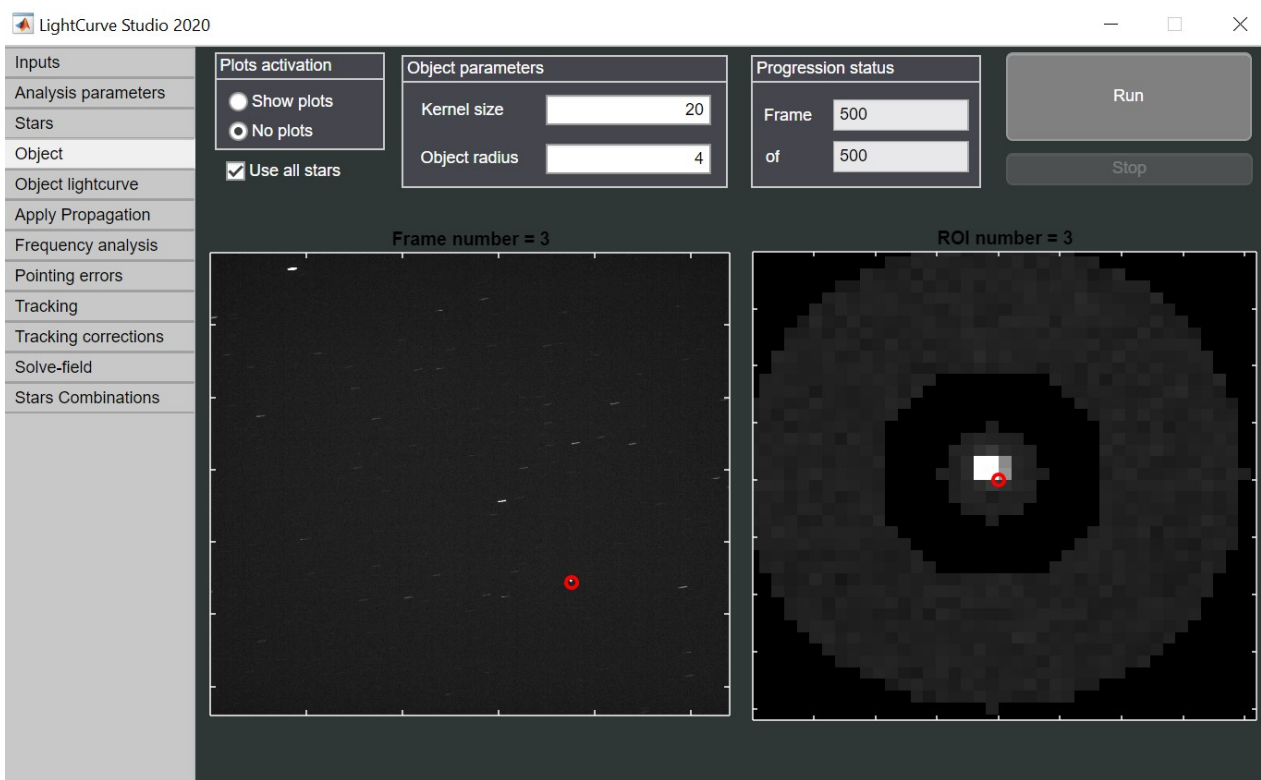
The parameters for image analysis are entered here. The user can choose whether to use a median filter and the size of its kernel, the spectral class of the stars to use and whether to calculate the background and the magnitudes using the mean or the median. It is also possible to select the optical tube used for the observation, and to use frames to calibrate the image.

4.5.3. Analysis parameters tab



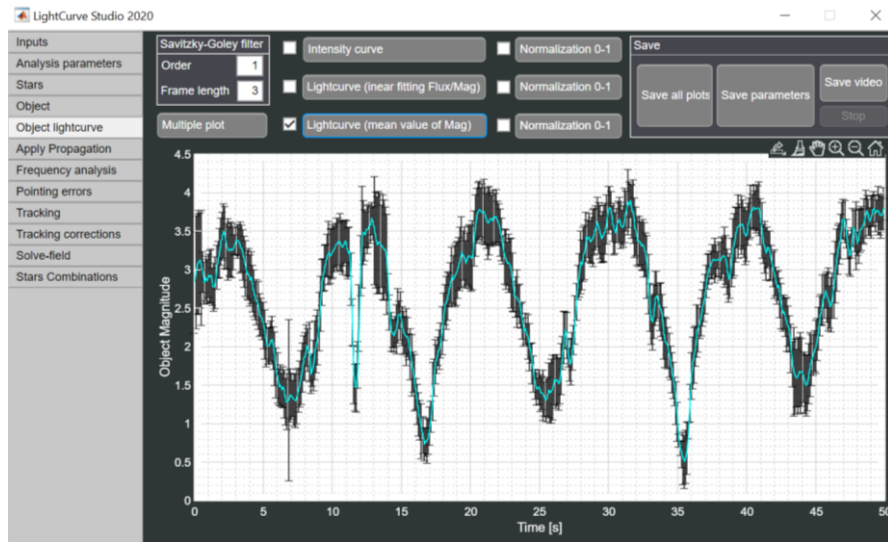
The magnitude of the stars is calculated as described in section 4.4. Thus, the difference between the catalog magnitude and the calculated magnitude can be visually represented. The dotted line shows the catalog magnitude, while the continuous line corresponds to the calculated one. Each of the stars found in the various frames is labeled with a different color, in order to distinguish the different stars.

4.5.4. Object tracking tab



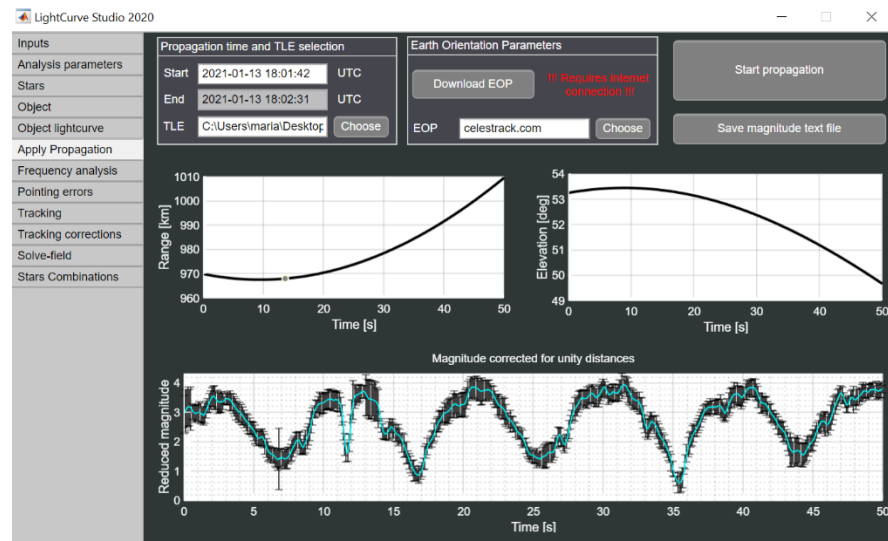
In this tab runs the algorithm for the optical tracking of the object, to determine the pixel coordinates of the object in each frame and its luminous intensity. Two parameters can be set, either for each frame or for the entire video, in order to improve the intensity estimate. They are the kernel size, that is the size of the sub-image in which the object is present, and the radius of the inner circle, which must be such as to contain the object while trying not to incorporate the background as well.

4.5.5. Object tracking tab



In this tab the light curve is retrieved. Therefore, the output graph shows the variation of the magnitude over time and also the relative error for each point of the curve, and thus an error plot. In particular, the blue curve represents the calculated magnitude, while the black lines show the error associated to each point. In the same plot, it is also possible to visualize the normalized curves, in terms of intensity or in terms of magnitude, between 0 and 1. These are then passed as an input to the attitude determination software.

4.5.6. Object tracking tab



Here the normalization of the light curve occurs. The output light-curve of the previous tab does not take into account the range-rate between the object and the observatory. Thus, a normalization with respect to the range is necessary. The obtained magnitude is called reduced magnitude and the effect of the normalization is shown in Fig.11 and Fig.12. Range and elevation of the object, during its passage over the observatory, are also shown as two different plots.

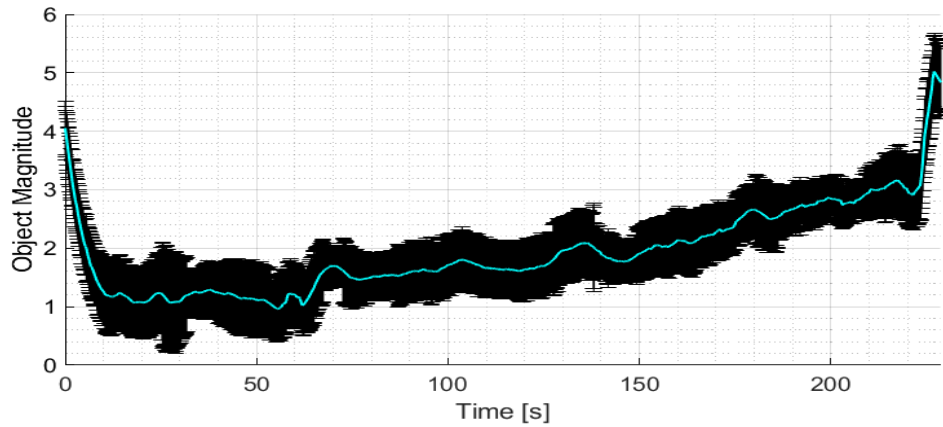


Fig. 11 - Observed light-curve not normalized of CZ-4C (SSN 40879) taken the 22nd of July 2020 from SCUDO observatory

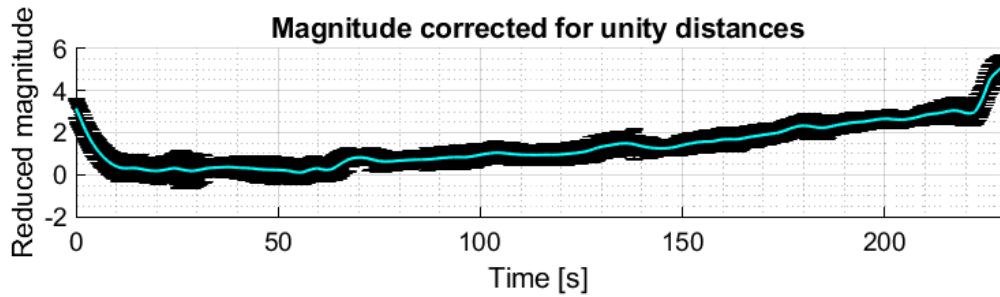
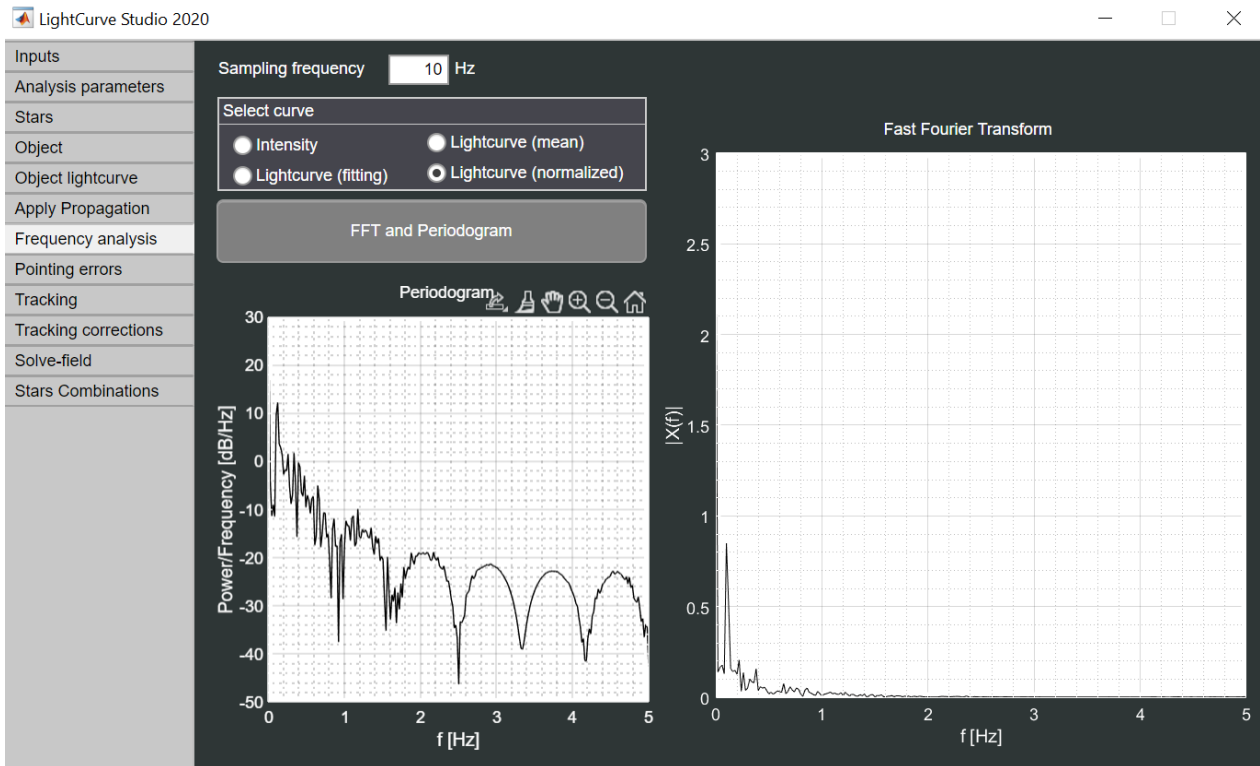


Fig. 12 - Observed normalized light-curve of CZ-4C (SSN 40879) taken the 22nd of July 2020 from SCUDO observatory. The decrease and the increase of the magnitude values respectively at the start and at the end of the tracking, represent the rise and the sets of the object.

4.5.7. Frequency analysis tab



In the frequency analysis tab, the Fast Fourier Transform (FFT) and the periodogram, which represent the spectral density, of the light curve are calculated to evaluate the possible presence of a dominant frequency. This type of analysis is important because it allows to estimate the light-curve period. In general, the light-curve period differs from the rotation period, but in particular situations where the optical axis and the main rotation axis coincide then the two periods are the same. This is the example of the observation of the Earth observation satellite SMAP during its passage over Colleparo (FR) of 2020-12-14 from 16:49:30 UTC to 16:53:27 UTC. In Fig. 13 is shown the satellite image and the FFT of the light-curve obtained during this passage. It is possible to see how the light-curve period and the period of the radiometer rotation is the same.

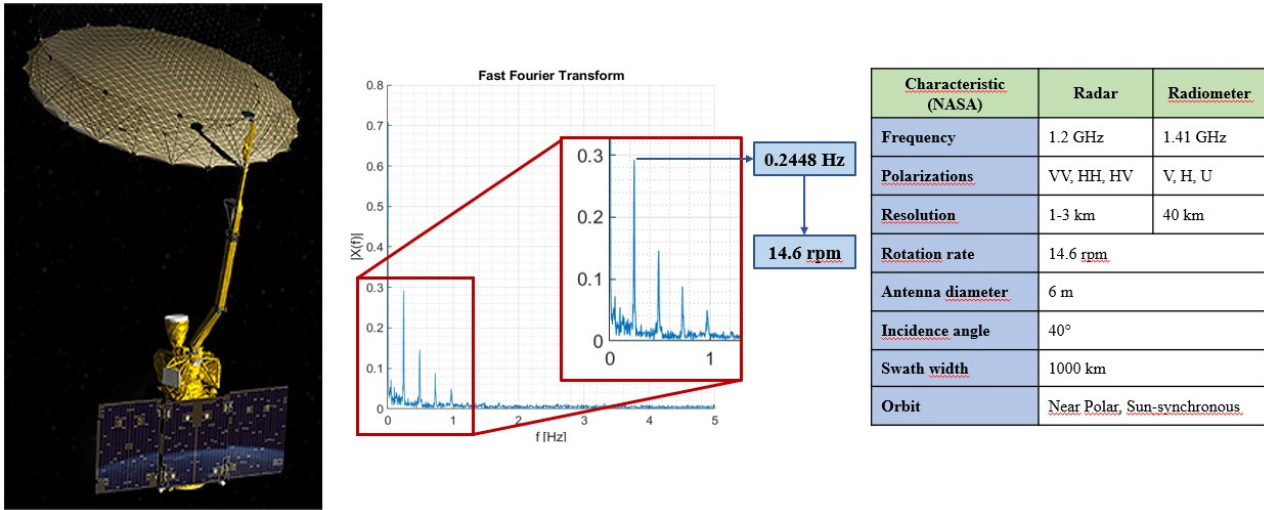
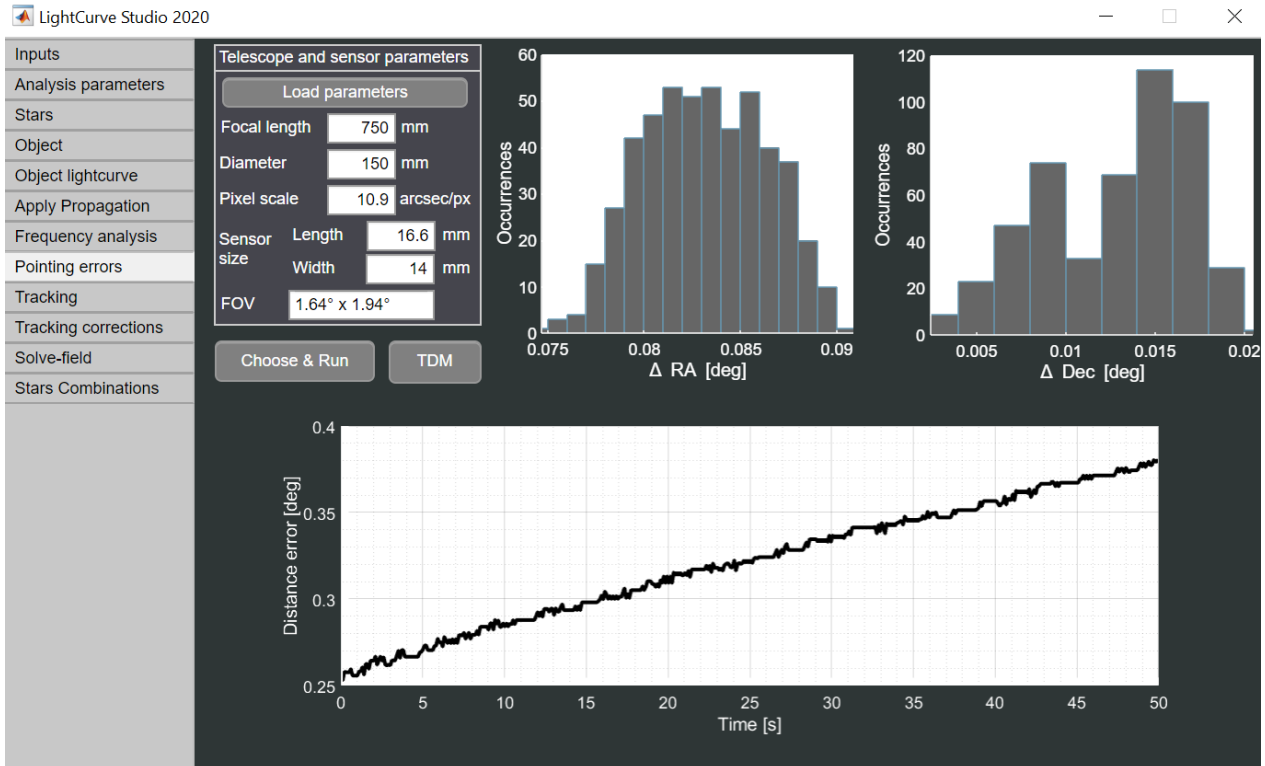


Fig. 13 – SMAP frequency analysis and the table with reported the main characteristics of the satellite provided by the NASA.

The knowledge of the light-curve period also permits to limit the search space of the genetic algorithm, as the angular velocity on a single principal axis of inertia can not be much greater than the light-curve period.

4.5.8. Pointing errors tab



In this tab the difference between the celestial coordinates, obtained through the resolution of the stellar field, and the coordinates obtained by propagating the TLE using David Vallado's SGP4 orbital propagator is calculated. These differences are reported in two different histograms. It is also calculated the difference, in terms of degrees, between the image center and the object position, in order to evaluate the sum of pointing error of the telescope and the error in the satellite position estimate.

5. Observation campaigns

To find the optimal shooting parameters, many tests were carried out. Mainly is necessary to check the binning, the exposure time, the frame rate, the image type (8, 12 or 16 bit) and whether to use global or rolling shutter. The main parameter to take under control is the exposure time, since a too high value of this means that the stars in the field of view are represented by too long strips with consequent failure in the resolution of the star field. Conversely, if a too short exposure time is used, not enough stars are identified for the astrometric resolution. Regarding the object, a high exposure time value could lead to a saturation of the pixels that represent the object in the field of view. Instead, a low exposure time value involves a lower signal to noise ratio of the object that make it not visible.

In Figure 14 are shown some examples of the light-curves taken both from SCUDO and RESDOS observatories recorded within the IADC campaign WG1 AI 38.2 “Attitude motion characterization of LEO upper stages using different observation techniques” [56], useful to validate the light-curve analysis software. This light curve are referred to the object PEGASUS R/B. The 3D model of these object are shown in Section 6.3.

Other upper stage recorded during this campaign are shown in Fig. 15. From these examples it is possible to see how the tumbling motion of these objects is quite smooth even showing a repetition period even if longer of the passage. The errors represented changes depending

on the actual state of the sky observed, so the error bars accommodate for every single measure to real observation situation.

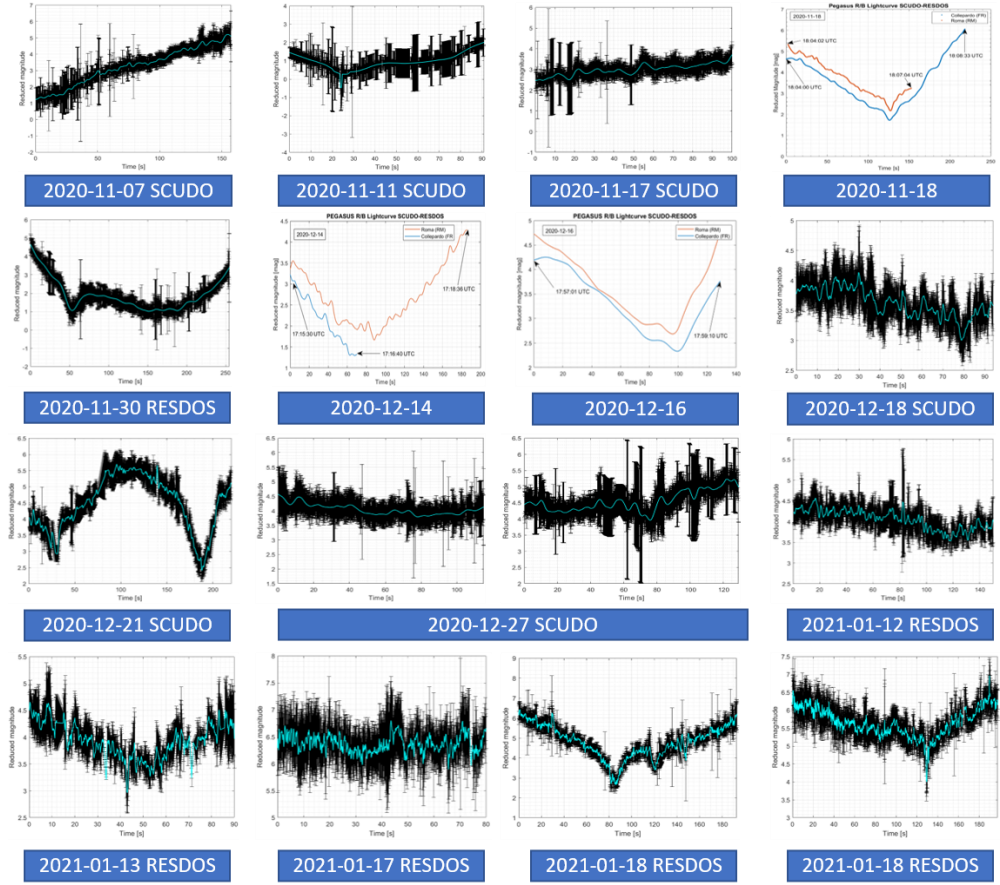


Fig. 14 – Recorded light-curve from November 2020 to January 2021 of Pegasus R/B.

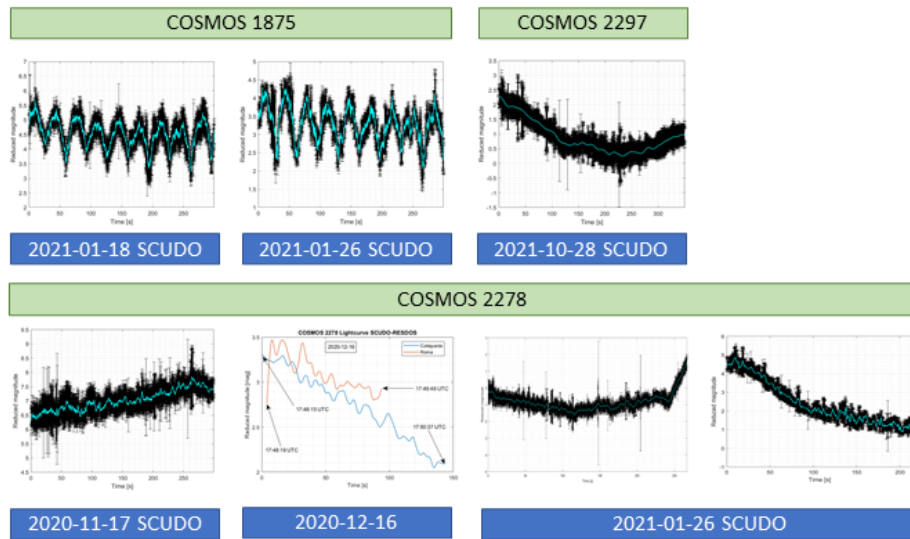


Fig. 15 - Light-curve of different upper stage recorded during the IADC campaign

Many tests were needed to calibrate the software parameters to get a correct calculation of the magnitude of the stars and the object and also to follow correctly the objects in the video frames. Once the software was validated, a simultaneous observation test was pursued. The Figure 16 shows an example of light-curves obtained during a bi-static observation taken from RESDOS and SCUDO observatories. In these plots the error is not represented for visualization purposes. The red curve is the light-curve obtained from RESDOS observatory, while the blue one from SCUDO observatories. The objects under consideration are both operative satellites and space debris. It is possible to notice how, even if the main behaviour is similar, some small differences are representative of different attitude of reflective faces with respect to the two observatories. These differences are of paramount importance in the process of light-curve inversion discussed later.

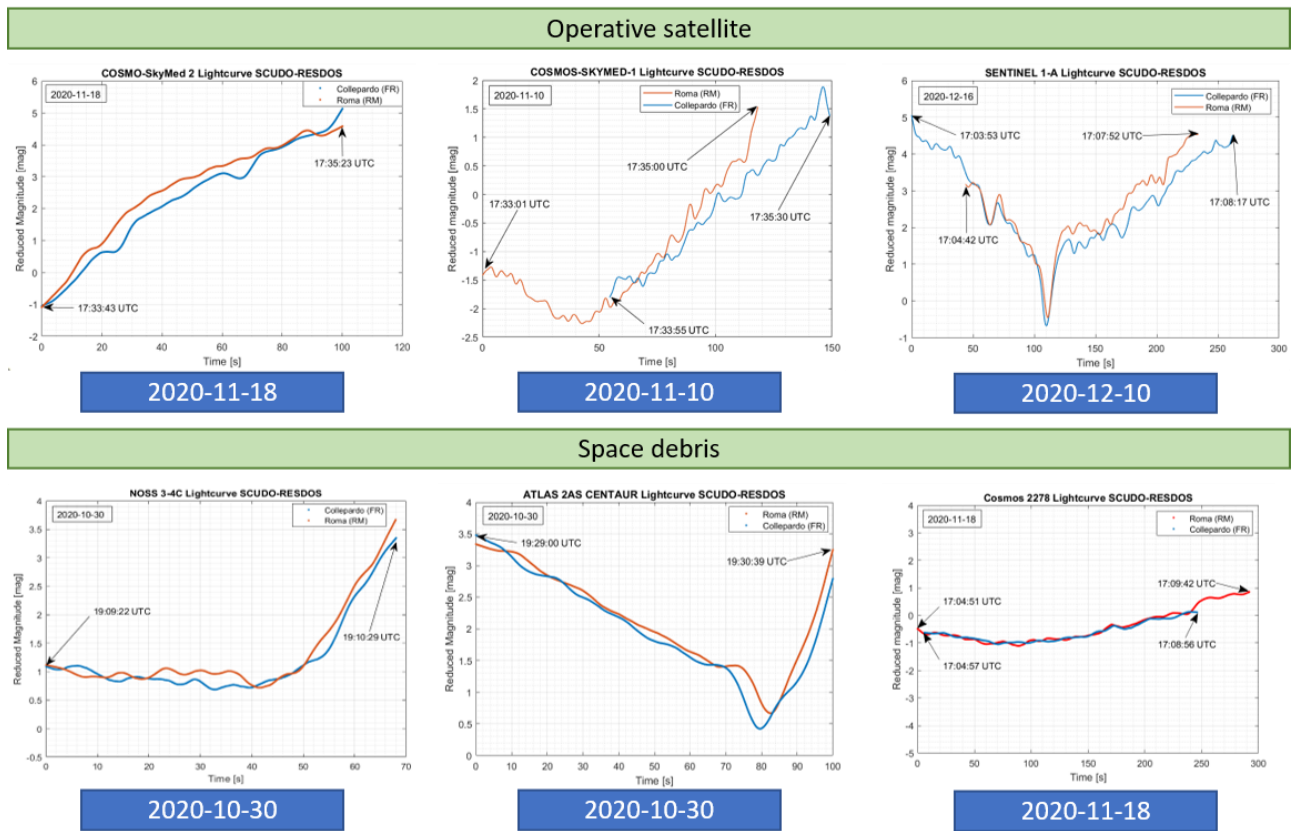


Fig. 16 - Operative satellites and space debris light-curve

The total number of the observation are shown in Tab. 3 while the observation for the IADC campaign in Tab. 4.

Total observations			
Observed objects	41	Space debris	18
		Operative satellites	23
Light-curves	95	Roma (RES DOS)	36
		Collepardo (SCUDO)	59
Simultaneous light-curves	20		

Tab. 3 – Total number of observations from XX to XX

IADC campaign	
Observed objects	5
Light-curves	26
Simultaneous light-curves	5

Tab. 4 – Total number of observations during the IADC campaign.

6. Attitude determination

The determination of the attitude is fundamental to understand the behavior of objects in orbit, especially for those not controlled and in the re-entry phase. The method proposed in this thesis foresees to compare the light curve obtained thanks to an optical observation with a synthetic one. The light curve of the object can be simulated using a virtual reality simulator through which the passage of the object over the observatory is reconstructed. Once the observed light curve is recovered from an optical observation, it can be compared with a synthetic one to see their similarity. Many synthetic light curves are generated with different initial attitude parameters. The closer the synthetic light curve is to the observed

one, the greater the probability that the corresponding attitude parameter represents the attitude of the real object. It is clear that the generator of synthetic light curves must be as realistic and reliable as possible both from an optic and a physical point of view.

- To reconstruct the orbit of the object, an SGP-4 (Simplified General Perturbation) routine is used in the range of interest.
- The position of the observer, the sun and the object are calculated for each instant in the same reference system.
- A 3D model of the object is required to generate a synthetic image.

The synthetic light curve represents the variation of the luminous flux reflected by the object over time, understood as the sum of the pixels of the image. Next, a genetic algorithm is used to minimize a cost function defined as the squared difference between the real light curve and the synthetic one. The algorithm tests different initial attitude parameters until both curves are similar.

6.1. Virtual Space Observation Engine (VISONE)

The virtual reality simulator takes into account numerous parameters and variables, both from an optical and physical point of view, such as atmospheric extinction, the shape and materials of the object, the phase angle between the sun-object-observer and the zones of shadow cast by the object on itself. A bad estimate of these parameters leads to an inaccurate synthetic light curve and therefore to an imprecise determination of the attitude. a specific virtual reality engine is therefore used for space observation simulations: the Virtual Space Observation Engine (VISONE). VISONE is composed of two main modules the physics engine and the rendering engine. Figure 17 shows a schematic of the VISONE engine.

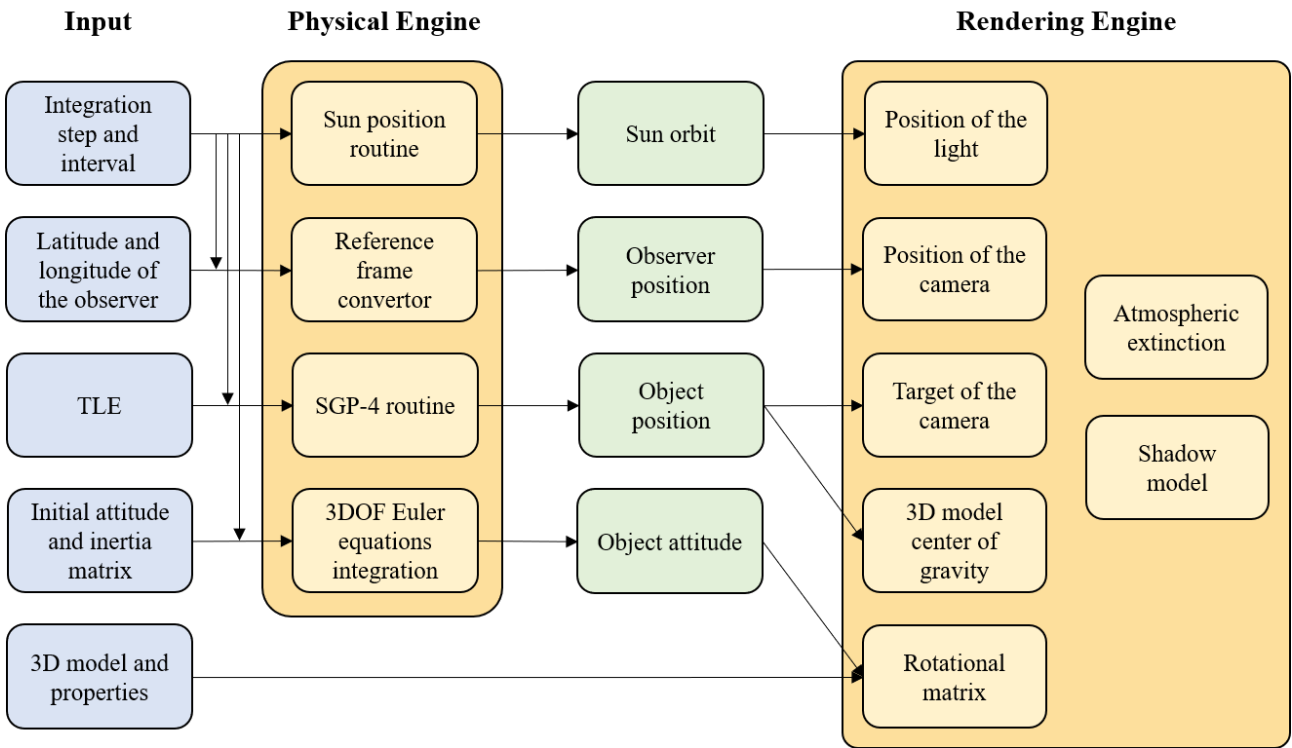


Fig. 17 – VISONE computes the position of the object and the sun in the same reference frame and renders on an image the 3D model of the orbital object as it should be seen by an observer on Earth.

The Physical Engine has the task of calculating, for each instant of time:

- Orbital position: the position of the object is computed using as input the TLE of the object. As mentioned in the introduction, the TLEs are characterized by low accuracy and short reliability therefore, the TLE closest to the measured time is chosen.
- Attitude: the classical Euler equation for a rigid body is used under the acceptable hypothesis of the null external torque since their effects on the object are negligible during the light-curve acquisition period. The dynamic state is represented by the Euler angle and the angular velocity components in the satellite reference frame $(\varphi_0, \theta_0, \psi_0, p_0, q_0, r_0)$. A specific matrix of inertia is considered for every type of object in order to consider the different geometry.
- Position of the observer: well known;
- Position of the sun: is computed using the ephemeris.

It is essential that all these positions are expressed in the same reference system, e.g., the Earth-Centered Inertial (ECI) one. With these parameters it is possible to calculate the phase angle (Fig. 18), which is fundamental for calculating the quantity of light reflected by the object.

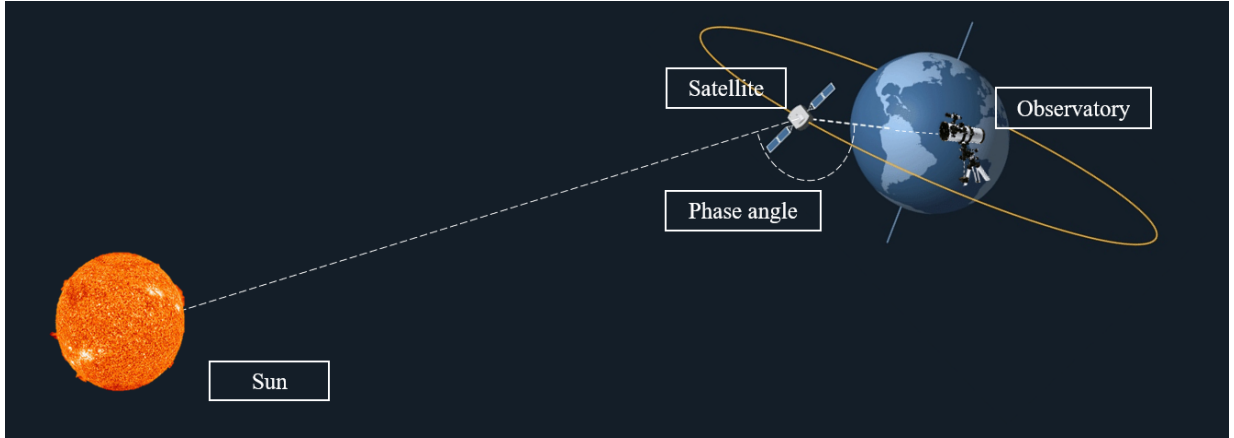


Fig. 18 - Phase angle – the image shows the phase angle, observer-object-sun, needed to compute the amount of light reflected by the object.

The rendering engine recreates a synthetic image of the object as realistically as possible. The outputs of the Physical Engine, the atmospheric extinction and the 3D model of the object are used as inputs in order to recreate the image of the object with also the shadows. The developed software uses the well-known loader library Assimp [57] making the software able to work with the most of material properties used in the 3D rendering field. The Blinn 'Phong light model [58] is used to recreate lighting conditions, whereas the shadows areas are modeled following the exponential shadow mapping model [59]. All these choices allow to be fast and precise in the light source computation, be they directional or far away, and in the evaluation of the light reflected by the object. In Fig. 19 are shown two examples of synthetic images produced by VISONE and showing also the correspondence between the real parameters with the model one.

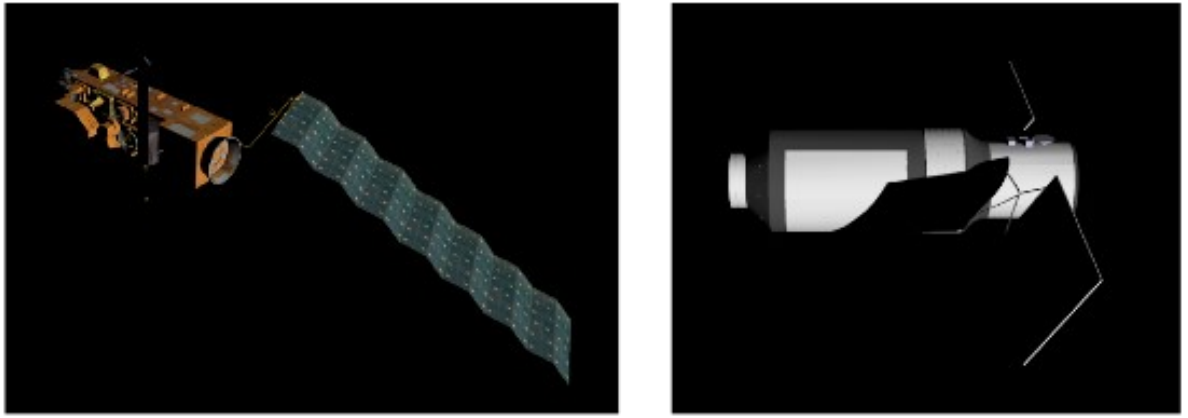


Fig. 19 - Rendered images - The figure shows the result of the rendering engine on the 3D model of the Tiangong-1 and Envisat with shadow.

6.2. Overview of the method

The real light-curve obtained depends only on the time t therefore it can be defined as $I_T(t)$. Instead, the synthetic one generated by VISONE depends not only on the time, but also on the initial attitude condition in terms of Euler angles and angular velocity components. Let be $\varphi_0, \theta_0, \psi_0$ the initial Euler angles and let be p_0, q_0, r_0 the initial angular velocities. The synthetic light-curve I_S can be defined as:

$$I_S(t, \varphi_0, \theta_0, \psi_0, p_0, q_0, r_0) \quad (5)$$

Therefore, it's possible to define a cost function as the sum over time of the modulus of the difference between the real and the synthetic light-curve:

$$\sum [I_T(t) - I_S(t, \varphi_0, \theta_0, \psi_0, p_0, q_0, r_0)]^2 \quad (6)$$

In this way the issue is reduced to a minimization problem in which the final task is to find the initial attitude parameters that generate the synthetic light-curve as close as possible to the real one. Those parameters will be the presumable attitude parameters of the observed

object. In this context a genetic algorithm [60] to solve the problem defined in Eq. 6 is used and the optimization architecture is shown in Fig. 20.

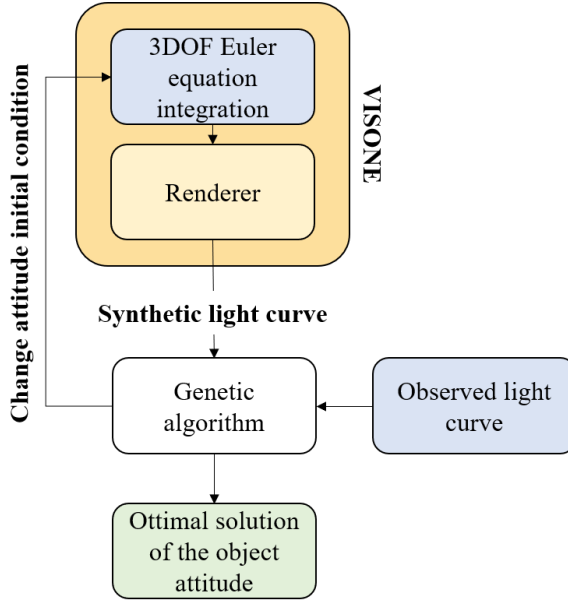


Fig. 20 - Optimization architecture – in figure it is shown the scheme of how the proposed method finds the attitude.

The used genetic algorithm is called GALGO that is a C++ template library designed to solve a problem under constraints (or not) by maximizing or minimizing an objective function on given boundaries (the details are explained in Appendix 3).

6.3. Simulation test

In order to validate the performance of the algorithm, many tests were carried out, placing ourselves in a situation as simple, but at the same time as realistic as possible. The body chosen to perform the tests is Cosmos 1875 (SSN 18334), which is the third stage of the Tsiklon-3 launcher [61]. The 3D model was retrieved from the NASA website [62], while the inertia matrix was assumed to be equivalent to that of a cylinder having the same mass and size of the object in question [63]. This approximation is due to the scarce availability of

information regarding the distribution of the masses of the model, which was also considered as axial-symmetrical.

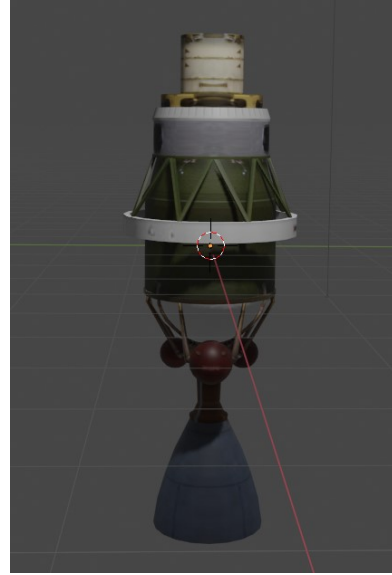


Fig. 21 – 3D model of Cosmos 1875

In the performed tests, a synthetic light-curve generated by VISONE from known attitude parameters was used in place of the real light-curve. The objective is to verify whether the genetic algorithm is capable to reconstruct the synthetic light-curve from the same known attitude.

The evolutionary parameters of the genetic algorithm and the constraints used for these tests are reported in Tab. 5.

Angular velocities	0.0 - 0.20	0.0 - 0.200	0.0 - 0.20
Euler angles	0.0 – 3.14	0.0 - 0.001	0.0 – 3.14
No. of chromosomes	5		
Selection	TRS		
Cross-Over	P1XO		
Mutation	UNM		
Target Energy	0.01		
No. of bits	5		

Tab. 5 – Constraints and evolutionary parameters for the first and second simulation test of Cosmos 1875.

The results of two representative optimization tests are shown in Fig. 22 and in Fig. 23, where it is possible to see how the proposed method found a compatible light-curve.

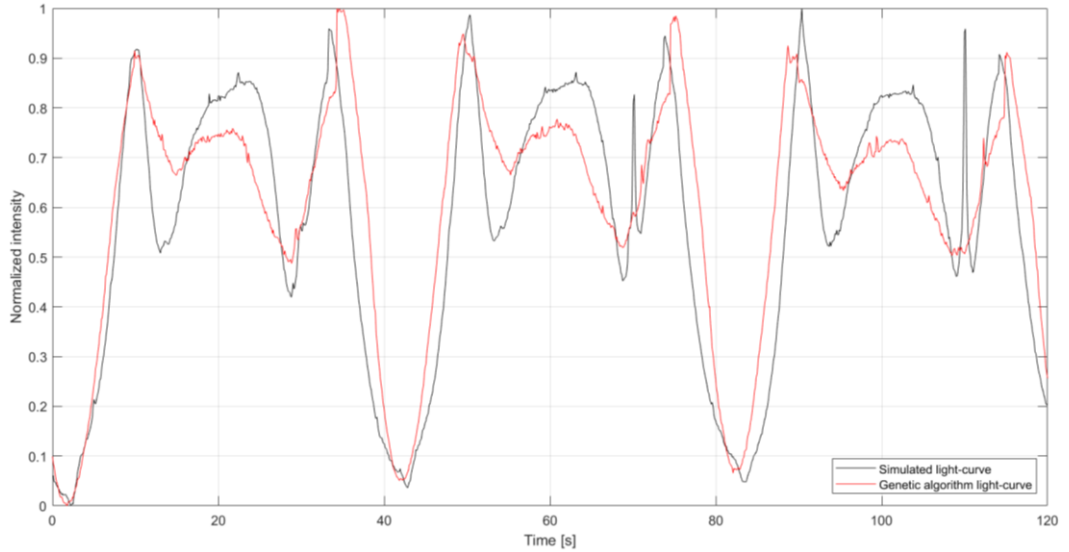


Fig. 22 – First simulation test using Cosmos 1875. In black is represented the simulated target light-curve obtained using VISONE and in red the light-curve obtained with the genetic algorithm optimization method.

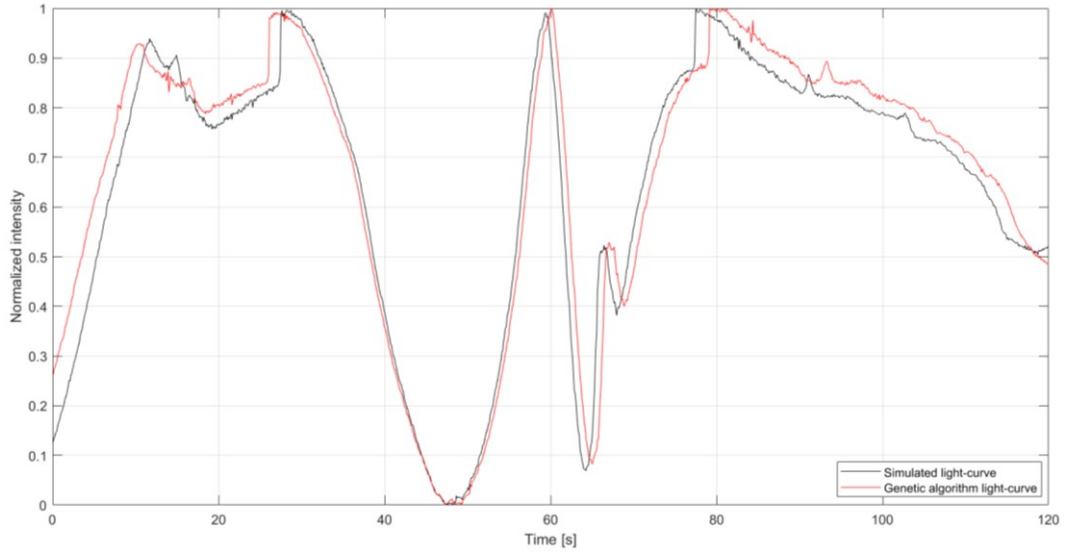


Fig. 23 – Second simulation test using Cosmos 1875. In black is represented the simulated target light-curve obtained using VISONE and in red the light-curve obtained with the genetic algorithm optimization method.

For the first and second tests, the found attitude parameters are reported in Tab. 6 and Tab. 7, respectively.

	Angular velocities [rad/s]	Euler angles [rad]
Target parameters	0.110 – 0.110 – 0.000	0.000 – 0.000 – 0.000
Found parameters	0.146 – 0.053 – 0.000	3.143 – 0.000 – 2.513

Tab. 6 – Target and found parameters for the first simulation test.

	Angular velocities [rad/s]	Euler angles [rad]
Target parameters	0.030 – 0.060 – 0.010	0.785 – 0.000 – 0.523
Found parameters	0.032 – 0.056 – 0.009	0.085 – 0.000 – 0.652

Tab. 7 - Target and found parameters for the second simulation test.

6.4. Real light-curve optimization

The object that was chosen for the optimization in the real case is PEGASUS R/B, since a great number of light-curves are recorded for this particular object. The light-curve used for the optimization is that of the 21-12-2020 recorded by SCUDO observatory starting from 18:02:19 UTC to 18:03:59 UTC. The used model is shown in Fig. 24 and its main characteristics are reported in Tab. 7.



Fig. 24 – 3D model of PEGASUS R/B.

Type	ORION 50 XL
Diameter	1.28 m
Length	3.07 m
Inert mass	391 kg
Launch mass	4306 Kg
Nozzle diameter	0.861 m

Tab. 8 – Main characteristics of PEGASUS R/B.

With this information, a simplified model (Fig. 25) was developed with the CATIA software in order to perform the inertia computation. The obtained inertia matrix is shown in Tab. 9.

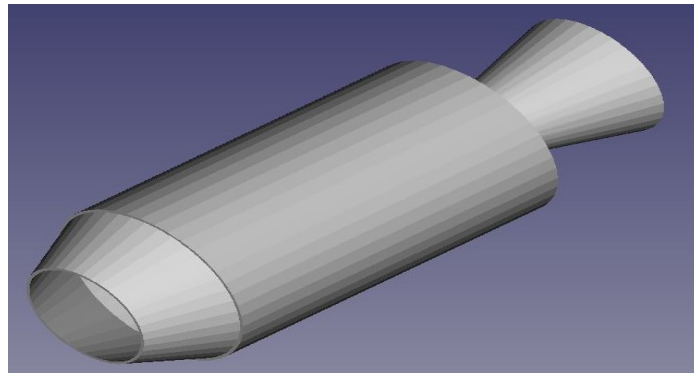


Fig. 25 – Simplified model of PEGASUS R/B used for the inertia computation.

Inertia matrix [kg*m^2]					
I_{xx}	1615.25	I_{xy}	0.00	I_{xz}	0.00
I_{yx}	0.00	I_{yy}	102.42	I_{yz}	-0.06
I_{zx}	0.00	I_{zy}	-0.06	I_{zz}	1615.25

Tab. 9 – Computed inertia matrix for the simplified model of PEGASUS R/B

The solution obtained with the genetic algorithm is shown in Fig. 26. In order to obtain this result, the algorithm runs 18482 tries, which correspond to about 4600 generations. The energy during the generations, and thus the square of the difference between the real and the synthetic light-curve, decreases from 0.1 to 0.014.

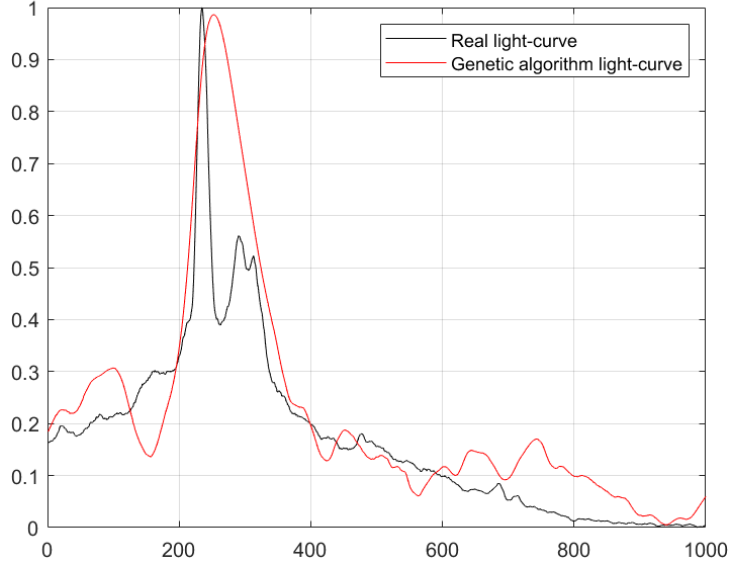


Fig. 26 - Real case: In black it is shown the real light-curve recorded 21-12-2020 recorded from SCUDO observatory and in red the light-curve generated by VISONE. In the x axis is represented the frame number that for 10 fps corresponds to 100 seconds, while in the y axis is present the normalized intensity.

The attitude parameters found for this case are reported in Tab. 10.

	Angular velocities [rad/s]	Euler angles [rad]
Found parameters	0.032 – 0.056 – 0.009	0.849 – 0.000 – 0.651

Tab. 10 – Attitude parameters found from the optimization of the real light-curve of PEGASUS R/B.

7. Conclusion

In this thesis, an in-depth method to retrieve light-curves has been shown. Despite the noise of the sCMOS sensor used for optical observation, the results prove that is possible to obtain a light-curve by means of an optical system. To achieve these results, star field resolution was performed, and the reference stars are selected to calculate the object's magnitude. Moreover, an optimization process that minimized the standard deviation with respect to several photometric parameters occurred. The whole process has been applied to a bi-static optical system, making it possible to obtain simultaneous data. Furthermore, a system for

the light-curve inversion based on a stochastic optimization (genetic algorithm) was identified, implemented, and tested in order to obtain compatible attitude motion from the light-curve obtained with optical ground-based measurements.

References

- [1] ESA. "Space Debris by the Numbers," European Space Agency. Available online: https://www.esa.int/Our_Activities/Operations/Space_Debris/Space_debris_by_the_numbers (accessed on 28 June 2018).
- [2] NSTCC. The National Science and Technology Council Committee on Transportation Research & Development; Interagency Report on Orbital Debris 1995; NSTCC: Washington, DC, USA, 1995.
- [3] Reihs, B.; McLean, F.; Lemmens, S.; Merz, K.; Krag, H. Analysis of CDM covariance consistency in operational collision avoidance. In Proceedings of the 7th European Conference on Space Debris, Darmstadt, Germany, 18–21 April 2017; ESA Space Debris Office:Darmstadt, Germany, 2017.
- [4] Adushkin, V.V. & Aksenov, O.Yu & Veniaminov, S.S. & Kozlov, Stanislav & Tyurenkova, Veronika. (2020). The Small Orbital Debris Population and its Impact on Space Activities and Ecological Safety. *Acta Astronautica.* 176. 10.1016/j.actaastro.2020.01.015.
- [5] Vallado, D.A.; McClain,W.D. Fundamentals of Astrodynamics and Applications, 3rd ed.; Microcosm Press/Springer: Hawthorne, CA, USA, 2007.
- [6] Vallado, D.; Cefola, P. «Two-line element sets-Practice and use». In Proceedings of the 63rd International Astronautical Congress, Naples, Italy, 1–5 October 2012; IAF: Paris, France, 2012. IAC-12,C1,6,12,x13640. Volume 7, pp. 5812–5825.
- [7] MehtaiD, P.M.; Kubicek, M.; Minisci, E.; Vasile, M. Sensitivity analysis and probabilistic re-entry modeling for debris using high dimensional model representation based uncertainty treatment. *Adv. Space Res.* 2017, 59, 193–211.

- [8] Acernese, M.; Zarcone, G. Improving accuracy of LEO objects Two-line elements through optical measurements. In Proceedings of the 69th International Astronautical Congress, Bremen, Germany, 1–5 October 2018. IAC-18,A6,9,8,x47421.
- [9] DiPrima, F.; Santoni, F.; Piergentili, F.; Fortunato, V.; Abbattista, C.; Amoruso, L. Efficient and automatic image reduction framework for space debris detection based on GPU technology. *Acta Astronaut.* 2018, **145**, 332–341.
- [10] Scire, G.; Piergentili, F.; Santoni, F. Spacecraft Recognition in Co-Located Satellites Cluster through Optical Measures. *IEEE Trans. Aerosp. Electron. Syst.* 2017, **53**, 1699–1708.
- [11] Piergentili, F.; Santoni, F.; Seitzer, P. Attitude Determination of Orbiting Objects from Lightcurve Measurements. *IEEE Trans. Aerosp. Electron. Syst.* 2017, **53**, 81–90.
- [12] Cardona, T.; Seitzer, P.; Rossi, A.; Piergentili, F.; Santoni, F. BVRI photometric observations and light-curve analysis of GEO objects. *Adv. Space Res.* 2016, **58**, 514–527.
- [13] Santoni, F. Dynamics of Spring-Deployed Solar Panels for Agile Nanospacecraft. *J. Aerosp. Eng.* 2015, **28**, 04014122.
- [14] Santoni, F.; Piergentili, F. Analysis of the UNISAT-3 Solar Array In-Orbit Performance. *J. Spacecr. Rocket.* 2008, **45**, 142–148.
- [15] Graziani, F.; Santoni, F.; Piergentili, F.; Bulgarelli, F.; Sgubini, M.; Bernardini, S. Manufacturing and Launching Student-Made Microsatellites: “Hands-on” Education at the University of Roma. In Proceedings of the 55th International Astronautical Congress of the International Astronautical Federation, the International Academy of Astronautics, and the International Institute of Space Law, Vancouver, BC, Canada, 4–8 October 2004; IAF: Paris, France, 2004.
- [16] Vaccari, L.; Altissimo, M.; Di Fabrizio, E.; De Grandis, F.; Manzoni, G.; Santoni, F.; Graziani, F.; Gerardino, A.; Pérennès, F.; Miotti, P. Design and prototyping of a micropropulsion system for microsatellites attitude control and orbit correction. *J. Vac. Sci. Technol. B Microelectron. Nanometer Struct.* 2002, **20**, 2793.

- [17] Marzioli, P.; Curiano, F.; Picci, N.; Piergentili, F.; Santoni, F.; Gianfermo, A.; Frezza, L.; Amadio, D.; Acerneese, M.; Parisi, L.; et al. LED-based attitude reconstruction and back-up light communication: Experimental applications for the LEDSAT CubeSat. In Proceedings of the 2019 IEEE 5th International Workshop on Metrology for AeroSpace (MetroAeroSpace), Torino, Italy, 19–21 June 2019; pp. 720–725. Aerospace 2021, 8, 4 18 of 18
- [18] Menchinelli, A.; Ingiosi, F.; Pamphili, L.; Marzioli, P.; Patriarca, R.; Msc, F.C.; Piergentili, F. A Reliability Engineering Approach for Managing Risks in CubeSats. Aerospace 2018, 5, 121.
- [19] Marzioli, P.; Gugliermetti, L.; Santoni, F.; Delfini, A.; Piergentili, F.; Nardi, L.; Metelli, G.; Benvenuto, E.; Massa, S.; Bennici, E. CultCube: Experiments in autonomous in-orbit cultivation on-board a 12-Units CubeSat platform. Life Sci. Space Res. 2020, 25, 42–52.
- [20] Hossein, S.H.; Acerneese, M.; Cardona, T.; Cialone, G.; Curianò, F.; Mariani, L.; Marini, V.; Marzioli, P.; Parisi, L.; Piergentili, F.; et al. Sapienza Space debris Observatory Network (SSON): A high coverage infrastructure for space debris monitoring. J. Space Saf. Eng. 2020, 7, 30–37.
- [21] Santoni, F.; Piergentili, F.; Cardona, T.; Curianò, F.; Diprima, F.; Hossein, S.H.; Canu, C.; Mariani, L. EQUO-Equatorial Italian Observatory at The Broglio Space Center For Space Debris Monitoring. In Proceedings of the 68th International Astronautical Congress, Adelaide, Australia, 25–29 September 2017. IAC-17,A6,IP,10,x38808.
- [22] Piergentili, F.; Ceruti, A.; Rizzitelli, F.; Cardona, T.; Battagliere, M.L.; Santoni, F. Space Debris Measurement Using Joint Mid-Latitude and Equatorial Optical Observations. IEEE Trans. Aerosp. Electron. Syst. 2014, 50, 664–675.
- [23] Piattoni, J.; Ceruti, A.; Piergentili, F. Automated image analysis for space debris identification and astrometric measurements. Acta Astronaut. 2014, 103, 176–184.
- [24] Porfilio, M.; Piergentili, F.; Graziani, F. Two-site orbit determination: The 2003 GEO observation campaign from Colleperdo and Mallorca. Adv. Space Res. 2006, 38, 2084–2092.

- [25] Scire, G.; Santoni, F.; Piergentili, F. Analysis of orbit determination for space based optical space surveillance system. *Adv. Space Res.* 2015, **56**, 421–428.
- [26] Piergentili, F.; Ravaglia, R.; Santoni, F. Close Approach Analysis in the Geosynchronous Region Using Optical Measurements. *J. Guid. Control. Dyn.* 2014, **37**, 705–710.
- [27] Kaasalainen, M.: Asteroid models from photometry and complementary data sources. In: American Institute of Physics Conference Series, Volume 1732 of American Institute of Physics Conference Series, p. 020003 (2016)
- [28] Kaasalainen, M., Torppa, J.: Optimization methods for asteroid lightcurve inversion. I shape determination. *Icarus* **153**, 24–36 (2001)
- [29] Kaasalainen, M., Torppa, J., Muinonen, K.: Optimization methods for asteroid lightcurve inversion. II the complete inverse problem. *Icarus* **153**, 37–51 (2001)
- [30] Kaasalainen, M., Torppa, J., Piironen, J.: Models of twenty asteroids from photometric data. *Icarus* **159**, 369–395 (2002)
- [31] Eapen, R.T., Frueh, C.: Averaged solar radiation pressure modeling for high area-to-mass ratio objects in geosynchronous orbits. *Adv. Space. Res.* **62**(1), 127–141 (2018)
- [32] Fruh, C., Kelecy, T., Jah, M.: Coupled orbit-attitude dynamics of high area-to-mass ratio (hamr) objects: Influence of solar radiation pressure, earth's shadow and the visibility in light curves. *Celest. Mech. Astron.* **117**(4), 385–404 (2013)
- [33] McMahon, J.W., Scheeres, D.J.: New solar radiation pressure force model for navigation. *J. Guid. Control Dyn.* **33**(5), 1418–1428 (2010)
- [34] Lynch, D., Russell, R., Rudy, R., Gutierrez, D., Turpin, M., Crawford, K., Dotan, Y., Kim, D., Skinner, M.: 3 - 13 μm spectra of geosynchronous satellites. In: The Advanced Maui Optical and Space Surveillance Technologies Conference, p. E81 (2006)
- [35] Seitzer, P., Abercromby, K., Barker, E., Rodriguez, H.: Optical studies of space debris at GEO – survey and follow-up with two telescopes. In: Advanced Maui Optical and Space Surveillance Technologies Conference, p. E37 (2007)
- [36] Schildknecht, T., Koshkin, N., Korobeinikova, E., Melikiants, S., Shakun, L., Strakhova, S., Linder, E., Silha, J., Hager, M.: Photometric monitoring of non-resolved space debris

and databases of optical light curves. In: Advanced Maui Optical and Space Surveillance Technologies Conference, p. 25 (2015)

- [37] Schildknecht, T., Musci, R., Fruh, C.P., Color, M.: Photometry and light curve observations of space debris in GEO. In: Advanced Maui Optical and Space Surveillance Technologies Conference, p. E51 (2008)
- [38] Schildknecht, T., Vannanti, A., Krag, H., Erd, C.: Reflectance spectra of space debris in GEO. In: Advanced Maui Optical and Space Surveillance Technologies Conference, p. E24 (2009)
- [39] Cowardin, H., Lederer, S., Liou, J.-C., Ojakangas, G., Mulrooney, M.: Optical signature analysis of tumbling rocket bodies via laboratory measurements. In: Advanced Maui Optical and Space Surveillance Technologies Conference, p. 61 (2012)
- [40] Scott, R., Wallace, B.: Satellite characterization using small aperture instruments at DRDC Ottawa. In: Advanced Maui Optical and Space Surveillance Technologies Conference, p. E36 (2008)
- [41] Hall, D., Hamada, K., Kelecy, T., Kervin, P.: Satellite surface characterization from non-resolved multi-band optical observations. In: Advanced Maui Optical and Space Surveillance Technologies Conference, p. 24 (2012)
- [42] Linares, R., Crassidis, J.: Dynamic observability analysis for attitude, angular velocity, shape, and surface parameters. In: 26th AAS/AIAA Space Flight Mechanics Meeting, pp. 2016–515 (2016)
- [43] Furfaro, R., Linares, R., Gaylor, D., Jah, M., Walls, R.: Resident space object characterization and behavior understanding via machine learning and ontology-based Bayesian networks. In: Advanced Maui Optical and Space Surveillance Technologies Conference, p. 35 (2016)
- [44] Linares, R., Jah, M., Crassidis, J.: Inactive space object shape estimation via astrometric and photometric data fusion. *Adv. Astronaut. Sci.* 143, 217–232, 01 (2012)

- [45] Linares, R., Jah, M., Crassidis, J., Leve, F.A., Kelecy, T.: Astrometric and photometric data fusion for inactive space object mass and area estimation. *Acta Astronaut.* 99, 1–15 (2014)
- [46] Cardona, T., Seitzer, P., Rossi, A., Piergentili, F., Santoni, F., BVRI photometric observations and light-curve analysis of GEO objects, (2016) *Advances in Space Research*, 58 (4), pp. 514-527. , DOI: 10.1016/j.asr.2016.05.025
- [47] Piergentili, F., Santoni, F., Seitzer, P., Attitude Determination of Orbiting Objects from Lightcurve Measurements, (2017) *IEEE Transactions on Aerospace and Electronic Systems*, 53 (1), art. no. 7819454, pp. 81-90. , DOI: 10.1109/TAES.2017.2649240
- [48] Santoni, F., Cordelli, E., Piergentili, F., Determination of disposed-upper-stage attitude motion by ground-based optical observations, (2013) *Journal of Spacecraft and Rockets*, 50 (3), pp. 701-708. DOI: 10.2514/1.A32372
- [49] Fabrizio Piergentili, Gaetano Zarcone, Leonardo Parisi, Lorenzo Mariani, Shariar Hadji Hossein and Fabio Santoni, LEO Object's Light-Curve Acquisition System and Their Inversion for Attitude Reconstruction, *Aerospace* 2021, 8(1), 4; doi:10.3390/aerospace8010004
- [50] Hogg, D.W.; Blanton, M.; Lang, D.; Mierle, K.; Roweis, S. Automated Astrometry, Astronomical Data Analysis Software and Systems XVII. Available online: <http://adsabs.harvard.edu/full/2008ASPC..394...27H> (accessed on 12 December 2020).
- [51] Høg, E.; Fabricius, C.; Makarov, V.V.; Urban, S.; Corbin, T.; Wycoff, G.; Bastian, U.; Schekendiek, P.; Wicenec, A. The Tycho-2 Catalogue of the 2.5 Million Brightest Stars; Naval Observatory: Washington, DC, USA, 2000.
- [52] Olson, T. The Colors of the Stars. In Proceedings of the Color Imaging Conference, Scottsdale, AZ, USA, 17–20 November 1998.
- [53] Howell, S. *Handbook of CCD Astronomy*, 2nd ed.; Cambridge University Press: Cambridge, UK, 2006.

- [54] Howell, S.B. Two-dimensional aperture photometry-Signal-to-noise ratio of point-source observations and optimal data-extraction techniques. *Publ. Astron. Soc. Pac.* 1989, 101, 616.
- [55] Stetson, P.B. On the growth-curve method for calibrating stellar photometry with CCDs. *Publ. Astron. Soc. Pac.* 1990, 102, 932.
- [56] IADC. Inter-Agency Space Debris Coordination Committee. Available online: <https://www.iadc-home.org/> (accessed on 1 June 2020).
- [57] Schulze, T.; Gessler, A.; Kulling, K.; Nadlinger, D.; Klein, J.; Sibyl, M.; Gubisch, M. Open Asset Import Library (Assimp). January 2012. Computer Software. Available online: <https://github.com/assimp/assimp> (accessed on 1 October 2020).
- [58] James, F. Blinn. Models of light reflection for computer synthesized pictures. In ACM SIGGRAPH Computer Graphics; ACM: New York, NY, USA, 1977; Volume 11, pp. 192–198.
- [59] Annen, T.; Mertens, T.; Seidel, H.; Flerackers, E.; Kautz, J. Exponential shadow maps. In Proceedings of Graphics Interface; Canadian Information Processing Society: Mississauga, ON, Canada, 2008; pp. 155–161.
- [60] Ponsich, A.; Azzaro-Pantel, C.; Domenech, S.; Pibouleau, L. Constraint handling strategies in Genetic Algorithms application to optimal batch plant design. *Chem. Eng. Process. Process. Intensif.* 2008, 47, 420–434.
- [61] Astronautix. <http://www.astronautix.com/t/tsiklon-3.html> (accessed on 1 March 2021).
- [62] NASA website. <https://nasa3d.arc.nasa.gov/models#D> (accessed on 1 March 2021).
- [63] Ailor, W., Hallman, W., Steckel, G., and Weaver, M., "Analysis of Reentered Debris and Implications for Survivability Modeling", in 4th European Conference on Space Debris, 2005, vol. 587, p. 539.
- [64] ANDOR website. <https://andor.oxinst.com/learning/view/article/comparing-scmos> (accessed on 4 February 2021)

Appendix A

8. CCD, EMCCD and sCMOS

The CCD and the CMOS are two different types of image sensors that have the same purpose, that of transforming a light signal into an analog or digital electronic signal that therefore it allows to reconstruct, process and store the framed image. These two types of sensors are among the most popular in the 21st century and find applications in the most diverse fields such as astronomy, microscopy, cell phone cameras and webcams. However, the CMOS sensor have a much more recent history than CCD, in fact only the recent miniaturization advances in the construction of integrated circuits and continuous research work have allowed CMOS sensors to become competitive from both a commercial and a commercial point of view performance compared to CCDs.

8.1. Charge-Coupled Device (CCD)

The observation of an orbiting object through a telescope positioned on the Earth's surface requires a sensor capable of operating with a very high sensitivity and a wide dynamic range. Additionally, the sensor is required to be able to record high frame rate events to achieve high temporal resolution. Often these requests are mutually exclusive as, for example, it is possible for a CCD to obtain a reduced RMS read noise ($< 3 \text{ e}^-$), but due to the serial read nature of CCDs, low read noise implies a low frame rate especially for sensors with different megapixel resolution. If, on the other hand, a CCD sensor is used at higher frame rates, one must necessarily sacrifice either the resolution and the field of view are sacrificed as there are fewer pixels per frame to read, or the reading noise and dynamic range. The inability to maintain low read noise at higher read rates renders the CCD unusable for optical tracking applications of low orbiting objects.

8.2. Electron Multiplier CCD (EMCCD)

Due to the mutual exclusivity between low reading noise and high frame rate the electron multiplier CCD (EMCCD) was induced. EMCCD cameras use an on-chip amplification mechanism called "impact ionization" which multiplies the photoelectrons generated in the silicon. This implies that the signal of a single product from a single photon can be amplified above the read noise, even at high frame rates. However, despite the sensitivity in extremely low light conditions, some drawbacks of the EMCCD technology remain. To better understand the difference in performance between CCD and EMCCD, consider a front-illuminated scientific CCD. These devices are able to achieve a frame rate of around 11 fps with a reading noise of around 6 electrons. The use of micro-lenses ensures that most of the incident photons are directed away from the interline metal screen and onto the active silicon area for each pixel, with a peak QE greater than 60%. The high performance combined with the low cost have made the leading-edge CCD a very popular choice. However, the aforementioned reading noise is too high for many scientific applications in low light conditions. Therefore, a higher dynamic range can only be achieved at slower frame rates (or small array sizes) with modest EM gain settings. Applying higher EM gain settings results in further reduction of the dynamic range. The sensor cost of EMCCD technology is an additional consideration, along with the practical restriction on resolution and field of view that accompanies the cost of the sensor. Currently, the largest commercially available EMCCD sensor has 1024×1024 pixel with a pixel size of $13\mu\text{m}$, representing a sensor area of 13.3×13.3 mm. This already entails a significant increase in costs.

8.3. Complementary Metal Oxide Semiconductor (CMOS)

The complementary metal oxide semiconductor (CMOS) are similar to CCD sensors in that they are semiconductor devices with photosensitive areas in each pixel that convert incident photons into electrons. CMOS technology was developed in the 1960s, but it wasn't until the mid-1990s that its development was not a priority due to the entry into the market of video cameras, mobile phones, automotive, computer vision, etc. that require a high volume of data. Each pixel site is a photodiode and three transistors, performing the functions of resetting or activating the pixel, amplification and charge conversion, and selection or multiplexing (Figure 2). The charge from the photosensitive pixel is converted to a voltage at the pixel site and the signal is multiplexed by row and column to multiple on chip digital-to-analog converters (DACs). Inherent to its design, CMOS is a digital device. This leads to the high speed of CMOS sensors, but also low sensitivity as well as high fixed-pattern noise due to fabrication inconsistencies in the multiple charge to voltage conversion circuits.

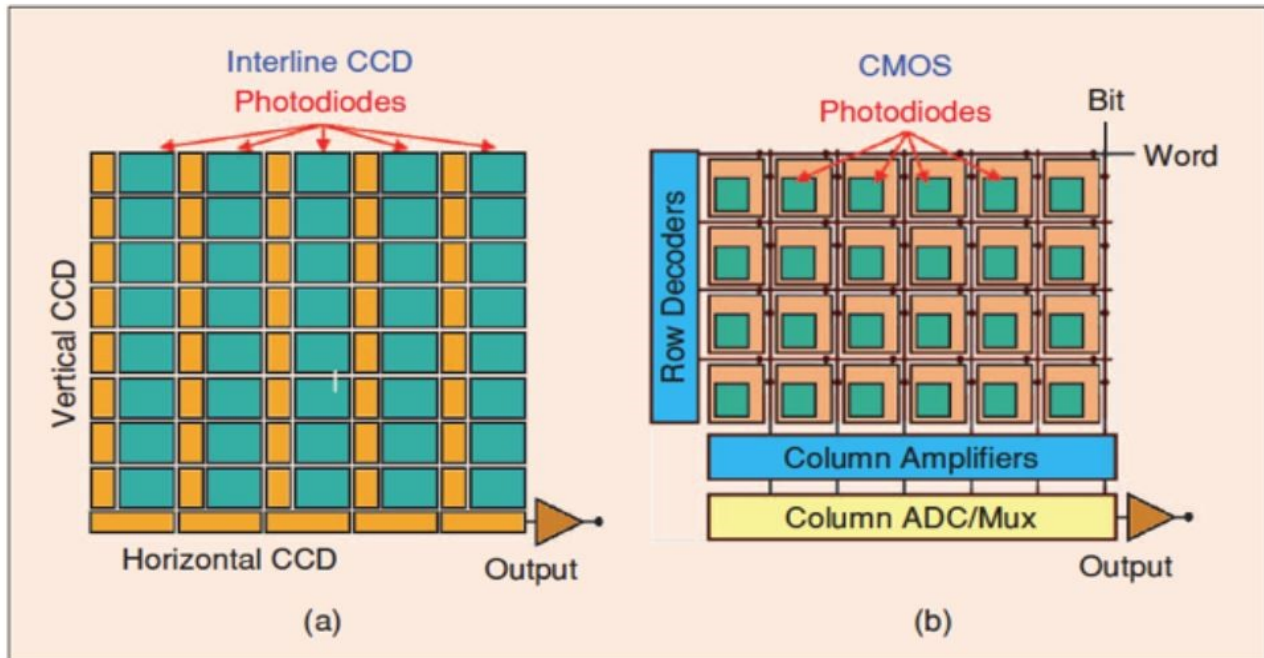


Fig. 27 - On the right is present a block diagram of a Complementary Metal Oxide Semiconductor (CMOS) and on the left the block diagram for an Interline CCD

Thanks to the multiplexing configuration it is possible to implement an roller or global electronic shutter. An additional advantage of a CMOS sensor is its low power consumption and dissipation compared to an equivalent CCD sensor, due to the lower charge flow or current. Furthermore, the CMOS has a better ability to handle high light levels without obtaining blooming and smearing phenomena characteristic in CCD sensors in which excess charge is transferred to adjacent pixels.



Fig. 28 - In the left is shown an image with blooming and on the right another image without blooming.

The main differences between CCD and CMOS sensors are shown in the following table.

	CCD	CMOS
Chip signal	Analog	Digital
Fill Factor	High	Moderate
Noise Level	Low	Moderate – High
Dynamic Range	High	Moderate
Uniformity	High	Low
Resolution	Low – High	Low – High
Speed	Moderate	High
Power Consumption	Moderate – High	Low
Complexity	Low	Moderate

Tab. 11 - Table of the main difference between CCD and CMOS sensors.

8.4. Scientific CMOS (sCMOS)

sCMOS (scientific Complementary metal–oxide–semiconductor) is a technology based on The next-generation of CMOS Image Sensor (CIS) is the sCMOS technologies, that offer low read noise, high frame rates, wide dynamic range, high quantum efficiency, high resolution, and a large field of view simultaneously in one image, without compromise. Although the reading noise of sCMOS is very low, the EMCCD technology still has a lower reading noise as well as having a quantum efficiency of up to 90% in the case of a backlit EMCCD. For these reasons, EMCCD technology is still preferable in low light applications that do not require high frame rates.

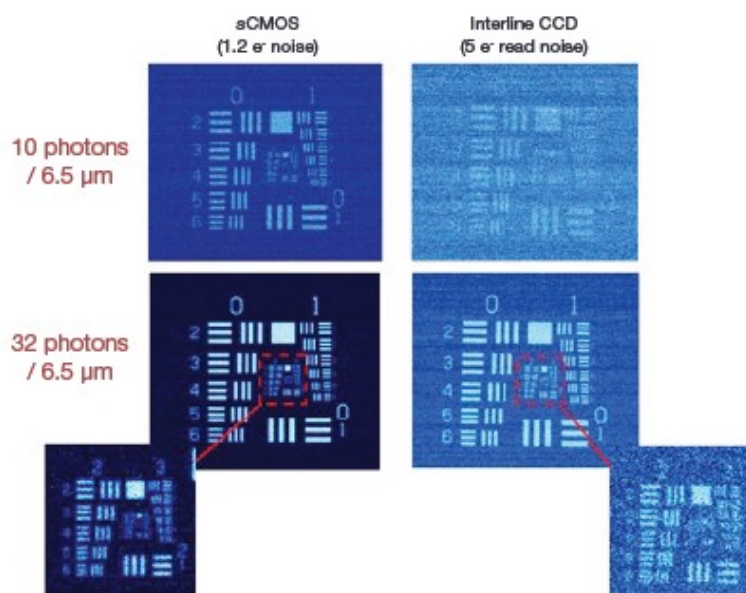


Fig. 29 - Comparative low light images of a USAF resolution chart, showing Andor sCMOS (1.3 electrons read noise @ 560 MHz) vs Interline CCD (5 electrons read noise @ 20 MHz), under the two lowest LED settings [64].

The superiority of sCMOS in terms of signal-to-noise ratio can be seen in this comparative exercise where specifications reflecting the most sensitive interline CCD and back-illuminated EMCCD sensors on the market today were used. The pixel size differences

between the two sensor types is negligible, thus there is no need to further correct for differing areas of light collection per pixel. The sensitivity differences between the two technology types is reflected in the marked variance between the respective SNR curves at low to moderate photon fluxes.

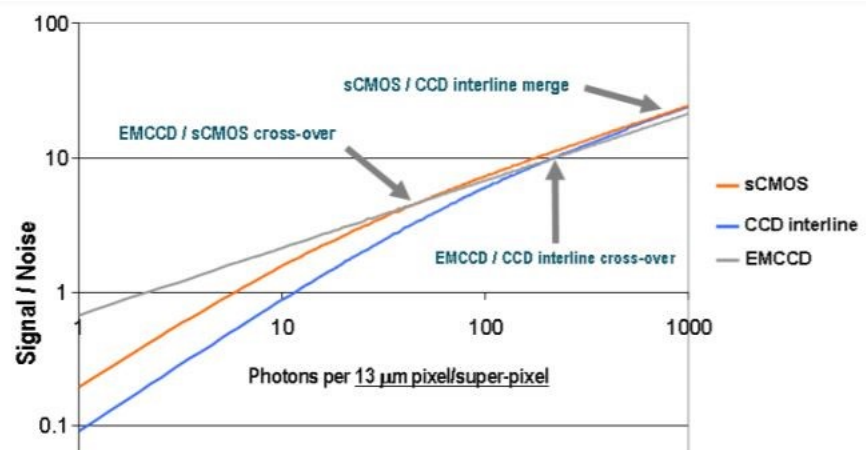


Fig. 30 - Theoretical Signal to Noise plot comparisons for sCMOS vs interline CCD vs back-illuminated EMCCD sensors [64].

Appendix B

9. Genetic Algorithm (GALGO 2.0)

The used genetic algorithm is called GALGO that is a C++ template library designed to solve a problem under constraints (or not) by maximizing or minimizing an objective function on given boundaries. This library is based on chromosomes represented as a binary string of 0 and 1 containing the encoded parameters to be estimated. It is possible to choose the number of bits N to encode each one of them within the interval [1,64]. When initializing a population of chromosomes, a random 64 bits unsigned integer (X), will be generated for each parameter to be estimated, X being inside the interval [0, MAXVAL] where MAXVAL is the greatest unsigned integer obtained for the chosen number of bits. If the chosen number of bits to represent a gene is N:

$$\text{MAXVAL} = 2^N - 1 \quad (7)$$

X will be then converted into a binary string of 0 and 1, the binary string will be truncated to the desired number of bits and added to the new chromosome. Once selection, cross-over and mutation have been applied, the new binary string obtained is decoded to get the new estimated parameter value Y. To do so, the binary string is first converted back into an unsigned integer X and the following equation is applied:

$$Y = \text{minY} + (X / \text{MAXVAL}) * (\text{maxY} - \text{minY}) \quad (8)$$

with minY and maxY representing the parameter boundaries. This method of generating a random ratio rather than a random real number allows to achieve faster convergence as only values inside the boundaries [minY, maxY] will be generated when initializing the chromosome population but also when recombining and mutating them. The step between two consecutive parameter values within the boundaries will be:

$$\text{step} = (\text{maxY} - \text{minY}) / \text{MAXVAL} \quad (9)$$

Estimating this step value before running the genetic algorithm is of high importance as it will greatly influence its performance. If the chosen number of bits N is large the algorithm will struggle to achieve fast convergence as the number of possible solutions within the boundaries will be too great, on the contrary, if it is too small the algorithm will struggle to find the global extremum and risk to quickly stall on a local extremum due to the lack of diversity within the chromosome population. The pre-existing methods to evolve a chromosome population contained are:

9.1. Selection methods

- Proportional roulette Wheel Selection (RWS): This could be imagined similar to a Roulette wheel in a casino. Usually a proportion of the wheel is assigned to each of the possible selections based on their fitness value. This could be achieved by dividing the fitness of a selection by the total fitness of all the selections, thereby normalizing them to 1. Then a random selection is made similar to how the roulette wheel is rotated.
- Stochastic Universal Sampling (SUS): SUS uses a single random value to sample all of the solutions by choosing them at evenly spaced intervals. This gives weaker members of the population (according to their fitness) a chance to be chosen. SUS starts from a small random number, and chooses the next candidates from the rest of population remaining, not allowing the fittest members to saturate the candidate space.
- Linear Rank-based Selection with selective Pressure (RSP)
- Classic linear rank-based selection (RNK): In rank-based fitness assignment, the population is sorted according to the objective values. The fitness assigned to each individual depends only on its position in the individuals rank and not on the actual objective value.
- Tournament Selection (TNT): In tournament selection a number *Tour* of individuals is chosen randomly from the population and the best individual from this group is selected as parent. This process is repeated as often as individuals must be chosen. These selected parents produce uniform at random offspring.
- Transform Ranking Selection (TRS): progresses from linear to nonlinear rank scaling during the evolution process according to a transform schedule.

9.2. Cross-Over methods

- One point cross-over (P1XO): A point on both parents' chromosomes is picked randomly, and designated a 'crossover point'. Bits to the right of that point are swapped between the two parent chromosomes. This results in two offspring, each carrying some genetic information from both parents.

- Two point cross-over (P2XO): In two-point crossover, two crossover points are picked randomly from the parent chromosomes. The bits in between the two points are swapped between the parent organisms.
- Uniform cross-over (UXO): In uniform crossover, typically, each bit is chosen from either parent with equal probability. Other mixing ratios are sometimes used, resulting in offspring which inherit more genetic information from one parent than the other.

9.3. Mutation methods

- Boundary mutation (BDM): This mutation operator replaces the genome with either lower or upper bound randomly. This can be used for integer and float genes.
- Single point mutation (SPM): A common method of implementing the mutation operator involves generating a random variable for each bit in a sequence. This random variable tells whether or not a particular bit will be flipped. This mutation procedure, based on the biological point mutation, is called single point mutation.
- Uniform mutation (UNM): This operator replaces the value of the chosen gene with a uniform random value selected between the user-specified upper and lower bounds for that gene. This mutation operator can only be used for integer and float genes.